# Moisture Budget Analysis of TOGA COARE Area Using SSM/I-Retrieved Latent Heating and Large-Scale $Q_2$ Estimates

SONG YANG AND ERIC A. SMITH

*Department of Meteorology and Supercomputer Computations Research Institute, The Florida State University, Tallahassee, Florida*

(Manuscript received 5 March 1997, in final form 29 July 1998)

ABSTRACT

This study addresses the retrieval of tropical open-ocean latent heating using Special Sensor Microwave Imager (SSM/I) satellite measurements. The analysis is carried out for the Tropical Ocean and Global Atmosphere Coupled Ocean–Atmosphere Response Experiment (TOGA COARE) intensive observation period in the western Pacific, much of it focused on the study area of the third WCRP–GPCP Algorithm Intercomparison Project (AIP-3) situated over the TOGA COARE Inner Flux Array (IFA). The retrieval algorithm is a profile-type physical inversion scheme based on the use of multispectral passive microwave (PMW) measurements. It estimates vertically distributed rain rate and latent heating by first retrieving mixing ratio profiles of liquid and frozen hydrometeors and then calculating rain fallout rates and vertical derivatives of the liquid–ice mass fluxes. Various modifications to the existing algorithm are discussed, including a combined visible–infrared–PMW–radar screening scheme for distinguishing among ''clear,'' ''cloud without rain,'' and ''cloud with rain pixels'' to better delineate vertical heating structure. Validation of retrieved rain rates over the AIP-3 study area indicates acceptable accuracy/precision uncertainty levels in terms of intensity, distribution, and time variation.

A procedure is developed for improving the initially retrieved heating profiles based on calibration to shipboard radar measurements. The modified algorithm and calibration scheme were applied to the IFA for estimating vertical profiles of latent heating. An optimum high-quality sounding period (1–17 February 1993) was selected for large-scale diagnostic calculations of apparent heating ($Q_1$) and moistening ($Q_2$) to analyze heat-moisture budgets of convective and stratiform cloud systems. Comparison and sensitivity tests indicate that the retrieved latent heating and $Q_1/Q_2$ calculations are representative. Moisture budget analyses over the IFA were carried out to study the detailed heating structures of clouds, particularly the cumulus scale heating process. This was accomplished by using residuals between the SSM/I-retrieved latent heating and the large scale $Q_2$ diagnostics. Results show that estimates of daily eddy vertical moisture flux divergence contain sizable uncertainties, however, by averaging over extended periods and vertically integrating to obtain surface latent heat flux transfer, close agreement to independently derived surface evaporation rates is found. This suggests that by combining the SSM/I retrievals with large-scale sounding data, it is possible to shed light on the role of cumulus convection on diabatic heating.

## 1. Introduction

It is well established that the diabatic heating distribution in both space and time represents an important thermal forcing mechanism in regard to monsoon circulations, tropical and midlatitude circulations, and the general circulation of the atmosphere. A number of studies (e.g., Puri 1987; Hack et al. 1989; Hack and Schubert 1990) have indicated that atmospheric circulations are sensitive to the detailed structure of the vertical heating profile. Both planetary-scale tropical circulations and interactions between the Tropics and higher latitudes change substantially with different heating profiles (Hartmann et al. 1984). The 30–60 day oscillation in the Tropics, which has a possible connection with the El Niño–Southern Oscillation (ENSO), is strongly affected by the shape and structure of the vertical heating profile (e.g., Lau and Peng 1987). Thus, determination of the temporal and spatial variations of vertical heating could be a vital aid for numerical weather and climate prediction.

Frank and McBride (1989) showed that there are differences between the life cycles of Atlantic and Australian convective disturbances. Maximum heating rates in Global Atmospheric Research Program Atlantic Tropical Experiment disturbances, throughout their life cycles, extend from the lower to upper troposphere. The altitudes of maximum heating in Australian Monsoon Experiment (AMEX) disturbances rise during their life cycles. Although it would be useful to determine whether or not there are similarities between the mean con-

*Corresponding author address:* Prof. Eric A. Smith, Department of Meteorology, The Florida State University, Tallahassee, FL 32306-4520.
E-mail: esmith@metsat.met.fsu.edu

© 1999 American Meteorological Society

Unauthenticated | Downloaded 12/05/23 04:44 PM UTC

vective heating profiles of AMEX and western Pacific ocean profiles, there are no similar data for the latter region. The western tropical Pacific is the area that contains large-scale atmospheric convergence associated with the ascending branch of the Walker circulation, superimposed with ascending motion driven by the western Pacific warm pool (Webster 1983). The convergence of air and moisture from the Pacific and Indian oceans leads to vigorous convection, heavy precipitation, and the release of latent heat in the atmosphere (e.g., Cornejo-Garrido and Stone 1977; Hartmann et al. 1984). Outgoing longwave radiation (OLR) variance analyses indicate that convective variability is situated mainly in the warm pools (e.g., Lau and Chan 1988). Lau and Chan (1986, 1988) also point out similarities between the dominant heating pattern associated with the 30–60 day oscillation and ENSO. They suggest that the 30–60 day oscillation and ENSO may be associated with the same type of intrinsic modes of variability, and that the former may act as a trigger for the onset of ENSO through the excitation of unstable coupled ocean–atmosphere modes, that is, a resonance phenomenon. Other OLR observations (e.g., Nakazawa 1988) have found that the greatest degree of convective organization and intensity is situated over the western Pacific warm pool region. The propagation of mesoscale convective systems may lead to the propagation of the warm pool itself, which can lead to changes in the general circulation.

Earlier studies (e.g., Houze 1982; Johnson 1984) showed that the heating profiles in precipitating stratiform and convective systems are different. The levels of maximum heating for these types of systems are located in the upper and lower troposphere, respectively. Heating profiles of different stratiform systems are generally consistent with one another from place to place. This is not the case for convective systems as other studies have shown that the heating profiles of the convective portion of storms vary significantly from place to place (Houze 1989). Therefore, it appears that the convective heating component is the main source of different heating profiles in different systems. In this regard, little is known about the details of the heating structure over the western Pacific warm pool area.

From the discussion in section 2d, it is evident that the quantities referred to as the apparent heat source ($Q_1$) and apparent moisture sink ($Q_2$) include contributions from cumulus-scale turbulent fluxes (i.e., vertical eddy heat and moisture fluxes), which cannot be obtained directly from observations. However, such fluxes can be estimated from observationally based diagnostic calculations (e.g., Nitta 1972; Yanai et al. 1973). Furthermore, numerical models can generate eddy flux profiles, such as presented by Tao et al. (1993a) in conjunction with the Equatorial Mesoscale Experiment (EMEX) and the Preliminary Regional Experiment for STORM Central (PRE-STORM). Although vertical flux profiles of total heating from diagnostic and modeling studies show general agreement, there are large differences in the lower troposphere between the EMEX region and the western Pacific. The vertical eddy fluxes represent important terms in the $Q_1/Q_2$ budgets, especially for convective clouds because of convective transports from the boundary layer. Furthermore, there are marked differences between the vertical eddy flux profiles of convective and stratiform clouds (Houze 1997).

Despite the importance of diabatic heating and its vertical structure, there is no direct measurement method for the heating profile. Indirect diagnostic methods have been developed but there are sparse opportunities for their application over the ocean because of the lack of adequate supporting datasets. On the other hand, satellite measurements provide a means to comprehensively survey the oceans, and are an important data tool for retrieving rainfall (Negri and Adler 1993; Wilheit et al. 1994; Smith et al. 1998). For example, satellite retrieved rain rates combined with surface observations are being used to provide global monthly rainfall estimates for the Global Precipitation Climatology Project (GPCP); Arkin and Xie (1994). Other studies have emphasized the role that passive microwave (PMW) satellite measurements can play in producing global datasets of rainfall (e.g., Ferraro et al. 1996). Satellite rainfall estimates are being applied to various research areas, such as climate diagnostic studies (e.g., Rasmusson and Arkin 1993), validation of rainfall forecasts from numerical weather prediction models (e.g., Janowiak 1992), and as input for surface process models (Shinoda and Lukas 1995). Rain rates derived from Special Sensor Microwave Imager (SSM/I) PMW measurements, and used for input to numerical prediction models, have resulted in better tropical storm forecasts (e.g., Chang and Holt 1994; Krishnamurti et al. 1994).

There are a number of different algorithms for retrieving precipitation over the ocean using visible (VIS), infrared (IR), and PMW satellite measurements, with the most physically appealing methods being the PMW algorithms (Wilheit et al. 1994; Smith et al. 1998). One of the advantages of using multispectral SSM/I measurements is that they provide information on the vertical microphysical structure of a cloud since the range of available SSM/I frequencies allows for differential penetration within the cloud column (Smith et al. 1992a). For that reason, PMW measurements are more effective than VIS and IR measurements in retrieving quantitative information on instantaneous rain-rate profiles and the associated latent heating profiles.

Generally, four different methods have been used to retrieve rain rates from PMW measurements (Smith et al. 1998). They are: 1) statistical rain map algorithms such as Berg and Chase (1992) and Ferraro and Marks (1995); 2) semiphysical rain map algorithms such as Adler et al. (1993) and Aonashi et al. (1996); 3) physical rain map algorithms such as Wilheit et al. (1991) and Bauer and Schluessel (1993); and 4) physically based

Unauthenticated | Downloaded 12/05/23 04:44 PM UTC

profile-inversion algorithms such as the iterative Florida State University (FSU) algorithm of Smith et al. (1994a,b) or the Bayesian GPROF algorithm of Kummerow et al. (1996). The profile-type algorithms have the advantage of providing the vertical variation of both rain rate and latent heating; see Smith et al. (1994c). Tao et al. (1990, 1993b) have shown, using a parameterized heating algorithm, that the retrieved latent heating profiles of convective cloud systems can be reliably estimated from satellite-retrieved profiles of hydrometeor liquid water content (LWC) and ice water content (IWC). These investigations included a case study from the western Pacific (Supertyphoon Thelma) based on retrievals from the FSU SSM/I profile algorithm (Smith et al. 1992b).

It is important to recognize that quantitative diagnostic studies concerning the accuracy of satellite-based latent heating profiles have not yet been carried out. This kind of study is important for future applications of PMW-based datasets, such as those that will be produced beginning in 1998 by the Tropical Rainfall Measuring Mission (TRMM); see Simpson et al. (1996). With this as the motivating factor, and using the FSU profile retrieval scheme discussed in section 2, we have conducted a quantitative error analysis of SSM/I-retrieved heating profiles, and estimates of the vertical eddy flux of moisture within the western Pacific warm pool.

The Tropical Ocean and Global Atmosphere (TOGA) Coupled Ocean–Atmosphere Response Experiment (COARE) is the most comprehensive experiment to date on the tropical warm pool atmosphere. One of the key features of this experiment is that it produced a high-quality dataset that can be used as ground truth for the calibration of satellite-retrieved precipitation. TOGA COARE took place in the heart of the western Pacific warm pool (Fig. 1). The intensive observation period (IOP) started on 1 November 1992 and continued through the end of February 1993; see Webster and Lukas (1992). The Integrated Sounding System (ISS), which combines state-of-the-art remote and in situ sensors into a single transportable facility, was used over the TOGA COARE intensive flux array (IFA) to obtain vertical soundings of temperature, moisture, and wind.

The foremost goals of this research are to demonstrate improvement in the current FSU SSM/I-based precipitation retrieval algorithm and the reliability of its application to the retrieval of tropical rain rate and latent heating profiles. Then, by using the retrieval algorithm in combination with the large-scale diagnostic budget scheme (such as described by Yanai et al. 1973) applied to TOGA COARE ISS measurements, the roles of vertical eddy heat and moisture fluxes on the heat–moisture budgets are investigated within the IFA. The specific scientific objectives of the study are 1) to modify and improve the current FSU retrieval algorithm, 2) to validate the retrieved rain rates and to develop a combined diagnostic scheme to calibrate the retrieved heating profiles over the third Algorithm Intercomparison Project (AIP-3) area situated over the IFA (see Ebert 1996, for discussion of AIP-3), 3) to apply the modified FSU algorithm and the heating calibration scheme to the TOGA COARE IFA area for retrieving latent heating, 4) to study the large-scale $Q_1/Q_2$ budgets for understanding heating and moistening processes, and 5) to explore the role of cumulus convection and turbulence on atmospheric moistening processes based on combining $Q_2$ estimates from ISS measurements and latent heating estimates from SSM/I retrievals.

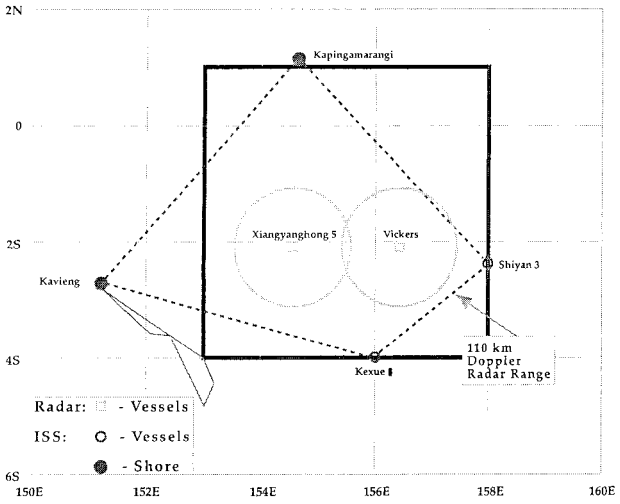


FIG. 1. Schematic diagram of TOGA COARE intensive flux array (indicated by dashed borders), showing locations and ranges of shipboard Doppler radars, with 5° square AIP-3 region outlined in bold.

## 2. Methodology

### *a. Current FSU precipitation profile retrieval algorithm*

The current FSU precipitation profile retrieval algorithm is based on the assumption that an explicit three-dimensional cloud model can be used to provide the microphysical underpinnings for an inversion-based retrieval procedure. The algorithm is a fully physical inversion technique designed to accept any combination of polarized or unpolarized satellite or aircraft passive microwave measurements. The algorithm uses basic multispectral radiative inversion concepts for scattering constituents, designed to retrieve the hydrometeor profiles of cloud, rain, precipitating, and nonprecipitating ice. The theoretical background for the algorithm has been discussed in the studies of Mugnai and Smith (1988), Smith and Mugnai (1988, 1989), Mugnai et al. (1990), Smith et al. (1992a), and Mugnai et al. (1993). The actual design of the algorithm for satellite applications has been described by Smith et al. (1994a,b), and for aircraft applications by Smith et al. (1994d). Smith et al. (1994c) has also provided an overview of

Unauthenticated | Downloaded 12/05/23 04:44 PM UTC

the conceptual and theoretical issues behind profile-type precipitation retrieval algorithms.

The FSU retrieval algorithm configured for SSM/I measurements consists of three key components: 1) cloud-radiation model calculations forming the initial guess database (Smith et al. 1994a); 2) spatially deconvolved SSM/I measurements at 19, 22, 37, and 85 GHz (Farrar and Smith 1992); and 3) a radiative transfer equation (RTE) model configured as a functional to an optimization scheme (Xiang et al. 1994; Smith et al. 1994a). The initial cloud microphysics used in the algorithm are based on 3D, nonhydrostatic mesoscale model output from the University of Wisconsin–Numerical Modeling System (UW–NMS); see Tripoli (1992a,b).

To initiate the retrieval processes, raw SSM/I satellite measurements at 19, 22, and 37 GHz are spatially enhanced to the resolution of the 85-GHz channels such that there is footprint conformity for all channels. Given the measured multispectral $T_B$'s at pixel coordinates, a selection process is applied to obtain initial guess profiles from the database needed by the RTE model for carrying out the inversion process. This involves applying the RTE model in a forward perturbative mode until there is an acceptable agreement between the modeled and measured $T_B$'s. The perturbation process is guided by a numerical optimization scheme (the golden-search method described in Gill et al. 1981), which generates a unique solution profile from a set of initial guess profiles.

The rainfall detection module is based on a modified version of the Grody (1991) screening scheme. The algorithm estimates vertical profiles of liquid and ice water contents [i.e., LWC($z$) and IWC($z$)], for precipitating raindrops and ice particles, as well as LWCs and IWCs for suspended cloud drops and ice particles. The vertical rain rate and mass flux profiles, as well as surface rain rates, are derived from gravity fallout equations consistent with those applied in the cloud model. The equivalent water content profiles of the two precipitating components are finally used to estimate latent heat profiles by evaluating the vertical derivative of the precipitation mass fluxes. The vertical rain-rate profile $\mathrm{RR}_{rd}(z)$ is given by:

$$\mathrm{RR}_{rd}(z) = -\rho_0(z)[\overline{W}_{rd}(z) + \overline{W}(z)]q_{rd}(z)/\rho_w, \quad (1)$$

where $\rho_0$ is basic-state air density, $\rho_w$ water density (1000 kg m$^{-3}$), $q_{rd}$ rain water mixing ratio, $\overline{W}(z)$ cloud-scale vertical velocity, and $\overline{W}_{rd}(z)_i$ vertically dependent mean terminal velocity,

$$\overline{W}_{rd}(z) = -1.94\left[\frac{4\rho_w D_{mw} g}{3C_{Dw}\rho_0(z)}\right]^{1/2}, \quad (2)$$

and $g$, $C_{Dw}$, and $D_{mw}$ are gravitational acceleration, water-drop drag coefficient (0.588), and characteristic diameter of raindrops (540 $\mu$m). The terms on the right-hand side are given in SI units whereas $\mathrm{RR}_{rd}$ is in mm s$^{-1}$. Applying Eq. (1) at $z = 0$ yields the surface rain rate.

A similar expression for precipitating ice particles is given by

$$\mathrm{RR}_{ip}(z) = -\rho_0(z)[\overline{W}_{ip}(z) + \overline{W}(z)]q_{ip}(z)/\rho_i, \quad (3)$$

where

$$\overline{W}_{ip}(z) = -\left[\frac{4\rho_i D_{mi} g}{3C_{Di}\rho_0(z)}\right]^{1/2}, \quad (4)$$

with ice particle drag coefficient, density, and characteristic diameter chosen as 0.45, 600 kg m$^{-3}$, and 1000 $\mu$m, respectively.

The mass flux profiles for raindrops ($R^*_{rd}$) and ice particles ($R^*_{ip}$) are given by

$$R^*_{rd}(z) = -[\overline{W}_{rd}(z) + \overline{W}(z)]\mathrm{LWC}_{rd}(z) \quad (5)$$

$$R^*_{ip}(z) = -[\overline{W}_{ip}(z) + \overline{W}(z)]\mathrm{IWC}_{ip}(z). \quad (6)$$

Without knowledge of the cloud-scale vertical velocity, the $\overline{W}(z)$ term can be set to 0. Finally, the latent heat profile ($Q$) due to condensation and deposition heating is given by

$$Q(z) = \frac{g}{c_p}\left[L_v\frac{\partial R^*_{rd}(z)}{\partial p} + (L_v + L_f)\frac{\partial R^*_{ip}(z)}{\partial p}\right], \quad (7)$$

where $L_v$ and $L_f$ are latent heats of vaporization and fusion, and $c_p$ is specific heat at constant $p$.

### b. Algorithm modifications

Although the current FSU algorithm has performed adequately in the past, for example, the National Aeronautics and Space Administration's WetNet PIP-1 Precipitation Intercomparison Project (Wilheit et al. 1994; Barrett et al. 1994), there are still areas in which improvements can be made. For example, the latent heat release calculations have been made only with respect to the precipitating hydrometeors without taking into account suspended hydrometeors. Furthermore, the effects of sea surface roughness and foam on sea surface emissivity have not been taken into account in the radiative transfer calculations. Since the effects of ocean surface roughness on surface emissivity are important during the precipitation detection phase of the algorithm, which is called ''screening'' (e.g., Grody 1991), they should be included in the algorithm. Because deconvolved SSM/I brightness temperatures are used in the study, we have applied a screening scheme developed from a dataset of spatially enhanced SSM/I brightness temperatures ($T_B$'s).

#### 1) Precipitation screen

The rule-based screening procedure of Grody (1991) was developed for detecting and identifying scattering surfaces (particularly rain) using a scattering index (SI)

Unauthenticated | Downloaded 12/05/23 04:44 PM UTC

approach, although the discriminant rules were not optimally developed for tropical oceans. Moreover, the SI threshold developed in Grody's analysis for detecting the presence of ocean precipitation is not applicable with deconvolved $T_B$'s, and thus does not lend itself to producing optimal results in the context of our IFA precipitation analysis in which we use spatially enhanced and spatially matched SSM/I $T_B$ measurements. Therefore, a modified precipitation screen was developed by taking advantage of high-resolution VIS and IR measurements from the Japanese Geosynchronous Meteorological Satellite (GMS), as well as shipboard C-band radar measurements from TOGA COARE, in conjunction with deconvolved SSM/I $T_B$'s over the IFA.

The basic philosophy of the new screen is to first exploit the high-resolution GMS measurements for identifying cloud-free SSM/I pixels, which are then used to develop an optimal SSM/I-based scattering index and SI precipitation threshold, which can be applied to an entire SSM/I scene for an initial test of the presence of precipitation. Furthermore, as additional assurance that only raining pixels are selected, we also use the shipboard radar reflectivities to identify a dataset of obviously raining SSM/I pixels to develop another set of rain indices (RIs), which are based on both polarization relationships and a differential frequency relationship at a common polarization. For purposes of this study, we developed two polarization-based RIs at 19 and 85 GHz, and one differential RI for 19 and 22 GHz at vertical polarization.

After analyzing histograms of GMS IR equivalent blackbody temperature (EBBT) and VIS albedo, we determined that an albedo value of 0.045 and EBBTs of 293 for daytime and 292 for nighttime are optimal for clear column detection. The selection process for clear column SSM/I pixels consists of two parts: 1) time match-up between the SSM/I swath and GMS observations, and 2) assurance that all GMS pixels within an SSM/I footprint satisfy the cloud-free criterion for both IR EBBTs and VIS albedos (albedo testing is only applicable for daytime). Since the SSM/I and GMS measurements over the AIP-3 study area were rarely synchronized in time, up to 10-min differences in the two types of observations were allowed during the selection procedure. Overall, 4185 clear sky SSM/I pixels were selected from the GMS procedure.

Raining SSM/I pixels over the AIP-3 study area were selected based on the shipboard radar measurements. This procedure was used only for the purpose of selecting undeniably raining SSM/I pixel samples needed for developing rain indices. An SSM/I pixel was considered to be raining only if all radar pixels located in the SSM/I pixel footprint indicated rain. Overall, 1710 raining SSM/I pixels were selected by this procedure.

Figure 2 (top panel) shows rms errors of estimated 85-GHz vertically polarized $T_B$'s using different combinations of lower-frequency vertically polarized channels over the AIP-3 study area for nonraining conditions.

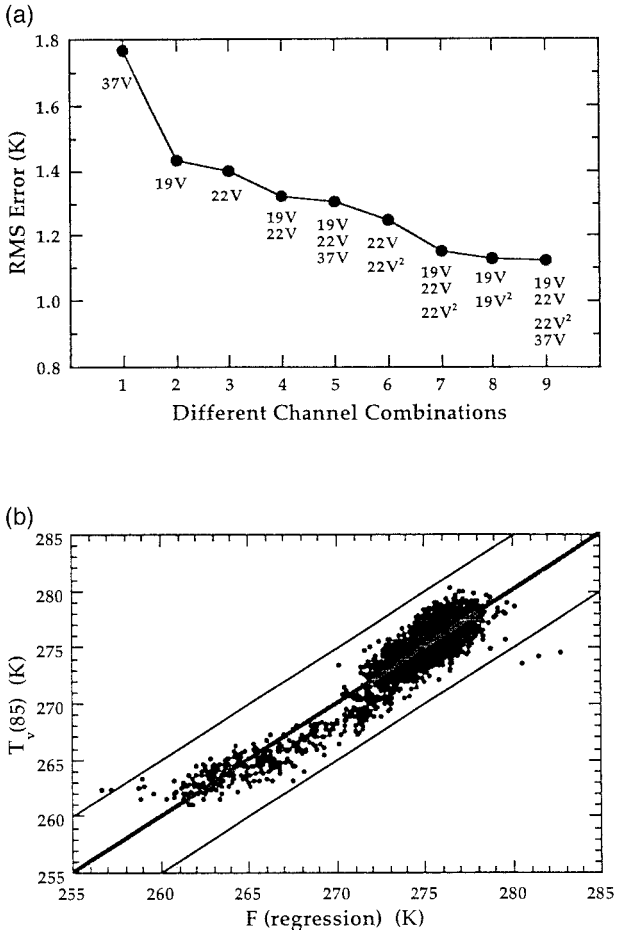


FIG. 2. Upper panel indicates rms errors for estimated 85-GHz vertically polarized clear sky SSM/I brightness temperature over AIP-3 study area using different combinations of lower-frequency channels. Lower panel indicates comparison of regressed and measured vertically polarized 85-GHz clear sky brightness temperatures over AIP-3 region.

To obtain these results, the clear-sky 85V measurements were regressed with nine different combinations of low-frequency vertically (V) polarized $T_B$'s. It is evident that the last three combinations (7th, 8th, and 9th cases) exhibit the most accurate estimates of 85V. The use of a single-channel estimation scheme is invariably inadequate. The use of 37V in combination with 19V–22V–22V$^2$ (9th case) gives the best results, exhibiting a slightly smaller error than the 19V–22V–22V$^2$ regression without 37V (7th case). The two errors are 1.12° and 1.15°C, respectively. However, since 37 GHz is more susceptible to scattering by nonprecipitating cloud than 19 and 22 GHz, 37V is not used to estimate 85V for nonscattering conditions. Thus the regression equation involving a combination of 19 and 22 GHz $T_B$'s used to estimate 85V $T_B$ in absence of scattering is given by

$$F = -843.1315313 + 0.379393T_v(19) + 8.0962867T_v(22) - 0.015671T_v(22)^2, \quad (8)$$

Unauthenticated | Downloaded 12/05/23 04:44 PM UTC

where $T_v(f)$ is a vertically polarized brightness temperature at frequency $f$. The bottom panel of Fig. 2 shows a comparison of estimates using Eq. (8) against measured 85V for 4185 clear-sky situations over the AIP-3 study area. The thin parallel lines are positioned $\pm 5$°C from the line of perfect agreement (thick line). It can be seen that only 5 of the 4185 clear-sky samples are located outside the $\pm 5$°C lines.

Since 19 and 22 GHz are relatively unaffected by scattering, any $T_B$ at 85V using Eq. (8) in the presence of scattering cannot be consistent with a measured 85V, which will be depressed by scattering. Therefore, following Grody (1991), a scattering index can be defined as,

$$\text{SI} = F - T_v(85), \tag{9}$$

where absolute index values greater than 5°C are used to identify scattering surfaces.

In order to further ensure an SSM/I pixel is raining, the RIs are introduced based on the fact that there are strong inter-relationships among the polarized $T_B$'s at 19, 22, and 85 GHz in the presence of rain. These relationships for the 1710 pixels unequivocally identified as raining are shown in Fig. 3. The thick lines are the regressions; the lack of scatter denotes the strong correlations. Correlation coefficients for the top, middle, and bottom panels are 0.996, 0.947, and 0.993, respectively, all significant at the 0.99 confidence level. The thin parallel lines in each panel are displaced $\pm 8$°, $\pm 6$°, and $\pm 8$°C from the thick lines, respectively. Only one pixel for the middle panel and two for the bottom panel lie outside of these lines. Hence, RIs for the 19, 22, and 85 GHz channels are given by

$$\text{RI}(19) = 133.38 + 0.51730T_H(19) - T_v(19), \tag{10}$$

$$\text{RI}(22) = 184.59 + 0.33855T_v(19) - T_v(22), \tag{11}$$

$$\text{RI}(85) = 9.4976 + 0.98180T_H(85) - T_v(85), \tag{12}$$

where RI values greater than 8°, 6°, and 8°C for the 19, 22, and 85 GHz tests are used to identify raining pixels. A detailed description of the development of this new screening scheme is found in Yang (1996). The new screening scheme identifies most of the raining pixels rejected by Grody's scheme over the Pacific warm pool.

### 2) Surface emissivity

Surface emissivity is affected by a variety of complicating factors including the ambient dielectric constant, surface roughness, and sea foam. There are a number of surface emissivity models used for different purposes. The model used here is based on the work of Stogryn (1971, 1972) and Lojou et al. (1994). In this context, the complete form of surface emissivity is given by

$$\varepsilon = (\varepsilon_s - \Delta\varepsilon_r)(1 - f_c) + \varepsilon_f f_c, \tag{13}$$

where $\varepsilon$ is the surface emissivity, $\varepsilon_s$ the specular emissivity, $\Delta\varepsilon_r$ the correction of emissivity due to surface roughness, $\varepsilon_f$ the emissivity of foam, and $f_c$ the foam coverage.

The effects of sea surface roughness and temperature on surface emissivity are significant and increase with frequency. The surface wind speed leads to an increase of surface emissivity, which is opposite the response to an increased SST. In general, a 10 m s$^{-1}$ variation of wind speed will change the surface emissivity at 19, 37, and 85 GHz about 4%, 5%, and 6%, respectively. Similarly, a 10° variation of SST will change the emissivity about 1%, 3%, and 5%, respectively.

### 3) Cloud-scale vertical velocity

A semiempirical scheme is used to express the cloud-scale vertical velocity. For this purpose, we make use of model output from a recent UW–NMS simulation for an intensifying tropical storm in the Caribbean basin. A detailed description of the simulation is found in the study of Panegrossi et al. (1998). Vertical velocity profiles and microphysical profiles for the five hydrometeor categories of cloud drops, raindrops, graupel particles, ice crystals, and snow flakes are used to establish a regression relationship between the microphysical parameters and the vertical velocities. Specifically, the vertical velocities generated from the simulation have been regressed against the hydrometeor concentrations used as independent variables, as a means to parameterize vertical velocity within a retrieval framework. The regression equation is

$$W_i = A_i + B_i\text{Cloud}_i + C_i\text{Rain}_i + D_i\text{Graupel}_i + E_i\text{Ice}_i + F_i\text{Snow}_i, \tag{14}$$

where $W$ is the regressed vertical velocity, while $A_i$, $B_i$, . . . , and $F_i$ are the regression coefficients (subscript $i$ indicates model level). All coefficients are listed in Table 1, in which the last column gives the correlation coefficients between the estimated and modeled vertical wind velocities. The correlation coefficients vary from 0.60 to 0.80, implying that the regressed vertical velocity in the column from 1 to 16 km can effectively represent the cloud-scale vertical velocity field. Since vertical velocities and hydrometeor concentrations are not well correlated below 1 km or above 16 km, but at the same time vertical velocities are small in those layers, the regressed vertical wind speed is set to zero below and above the 1 and 16 km levels.

Figure 4 (top panel) shows the biases and rms's between the regressed and modeled vertical velocities. The magnitudes in the bias profile are very small. The rms's are also small with a maximum value of 1.6 m s$^{-1}$ located around the 10-km height surface. One example of a comparison between the estimated and modeled vertical wind profiles is given in the bottom panel of Fig. 4. This shows that the estimated vertical velocities adequately describe the structure and magnitude of the vertical wind profile. Note that explicit updrafts and

Unauthenticated | Downloaded 12/05/23 04:44 PM UTC

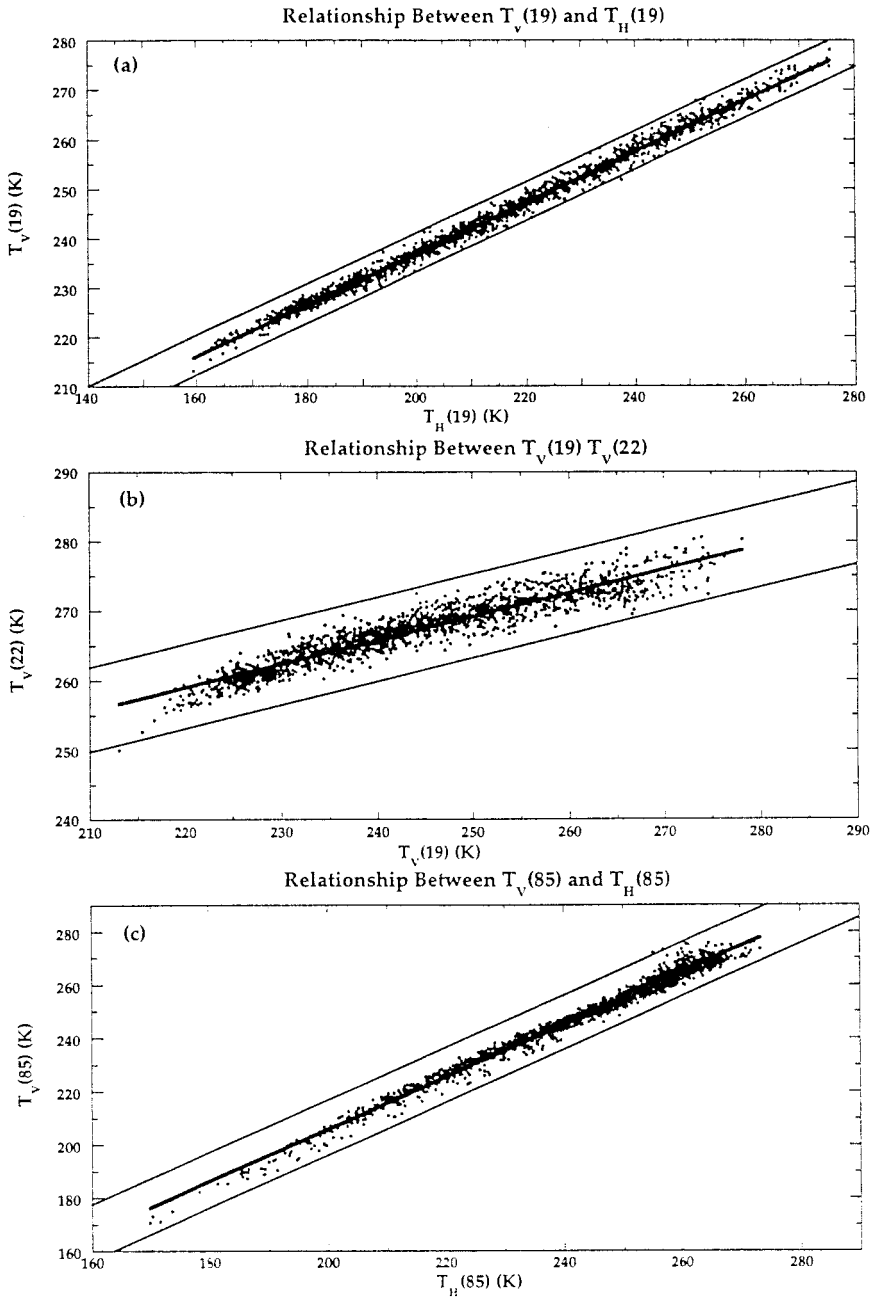


FIG. 3. Relationships between vertically (V) and horizontally (H) polarized SSM/I brightness temperatures for raining pixels over AIP-3 study area at different frequencies (raining pixels identified from TOGA COARE C-band radar measurements). These distributions have been used to develop two polarization-based rain indices at 19 and 85 GHz (i.e., from panels a and c), and one differential frequency-based rain index at common polarization using 19 and 22 GHz (from panel b).

downdrafts of rain environments are not addressed during the rain retrieval process because at the SSM/I pixel resolution, such processes cannot be resolved. Moreover, the hydrometeor database from the cloud model does not well resolve the explicit updraft–downdraft structure because the simulation was not run at an ideal cloud-resolving scale. Thus, the cloud vertical velocity used here represents a mean value over an SSM/I measurement footprint.

The effect of incorporating the estimated cloud-scale vertical velocity on the rain rate and heating profiles can be seen from Eqs. (1), (3), and (7). This indicates that although the cloud liquid water content redistribution caused by the vertical velocity adjustment does

Unauthenticated | Downloaded 12/05/23 04:44 PM UTC

TABLE 1. Regression coefficients for cloud, rain, graupel, ice crystals, and snow used to estimate vertical velocity at 18 model levels (heights indicated in km) from hydrometeor concentrations. Units of regression coefficients are (m $s^{-1}$) (g $m^{-3}$)$^{-1}$, with *y*-intercept (in m $s^{-1}$) also indicated. Final column indicates correlation coefficients (*r*'s) associated with individual level-dependent regressions.

| Level | Height | Intercept | Cloud | Rain | Graupel | Ice | Snow | *r* |
|---|---|---|---|---|---|---|---|---|
| 4 | 1.076 | −0.0895 | 3.8000 | 0.0460 | 0.0000 | 0.0000 | 0.0000 | 0.6440 |
| 5 | 1.584 | −0.1897 | 3.1067 | 0.0820 | 0.0000 | 0.0000 | 0.0000 | 0.6798 |
| 6 | 2.142 | −0.2345 | 2.9362 | 0.1362 | 0.0000 | 0.0000 | 0.0000 | 0.6741 |
| 7 | 2.757 | −0.2756 | 2.9101 | 0.2158 | 0.0000 | 0.0000 | 0.0000 | 0.6774 |
| 8 | 3.432 | −0.2878 | 2.7781 | 0.3432 | 0.0000 | 0.0000 | 0.0000 | 0.6756 |
| 9 | 4.175 | −0.0708 | 2.2475 | 0.8176 | −3.4165 | 0.0000 | −14.722 | 0.7664 |
| 10 | 4.993 | −0.1106 | 2.8597 | 1.2723 | −0.7004 | 9.9508 | −0.0548 | 0.7951 |
| 11 | 5.894 | −0.1018 | 0.0000 | 3.5005 | 0.3475 | 12.4881 | 1.6478 | 0.7272 |
| 12 | 6.871 | −0.4738 | 0.0000 | 0.0000 | 1.0725 | 8.3090 | 2.0783 | 0.7091 |
| 13 | 7.875 | −0.7749 | 0.0000 | 0.0000 | 1.5781 | 1.9476 | 3.5094 | 0.7525 |
| 14 | 8.875 | −0.9571 | 0.0000 | 0.0000 | 2.1629 | 1.2059 | 4.2715 | 0.7569 |
| 15 | 9.875 | −1.2230 | 0.0000 | 0.0000 | 2.8494 | 1.5882 | 4.7481 | 0.7424 |
| 16 | 10.875 | −1.5557 | 0.0000 | 0.0000 | 3.4500 | 2.3101 | 5.1494 | 0.7239 |
| 17 | 11.875 | −1.5368 | 0.0000 | 0.0000 | 3.8904 | 2.6373 | 5.6360 | 0.7135 |
| 18 | 12.875 | −1.3135 | 0.0000 | 0.0000 | 4.3241 | 2.7674 | 6.1467 | 0.7137 |
| 19 | 13.875 | −0.9283 | 0.0000 | 0.0000 | 5.0189 | 2.5004 | 6.5519 | 0.7176 |
| 20 | 14.875 | −0.5334 | 0.0000 | 0.0000 | 6.4752 | 1.9613 | 6.4258 | 0.7146 |
| 21 | 15.875 | −0.1952 | 0.0000 | 0.0000 | 8.5993 | 1.2467 | 5.2299 | 0.5967 |

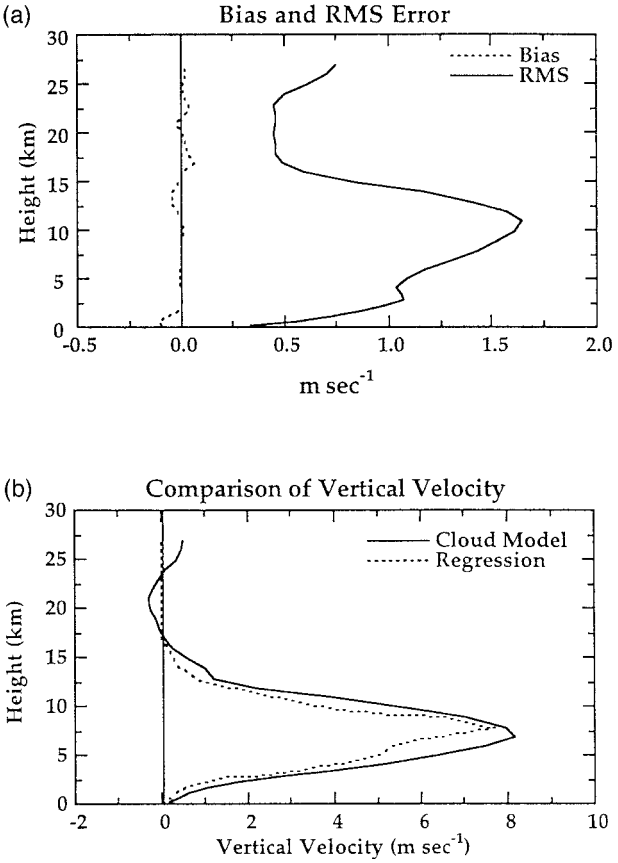


FIG. 4. Upper panel indicates bias and rms error profiles between regressed and modeled vertical velocities. Regressed vertical velocity is based on cloud model-generated concentrations for cloud, rain, graupel, ice crystal, and snow hydrometeors. Lower panel provides one example of comparisons between regressed and modeled vertical velocities.

not contribute to any net heating, it does adjust the vertical structure of the latent heating profile. This will be discussed further in section 5a.

Given a cloud-scale vertical velocity, the mass flux profile for cloud drops ($R^*_{cd}$) is

$$R^*_{cd}(z) = -\overline{W}(z)\mathrm{LWC}_{cd}(z). \tag{15}$$

Therefore, total latent heating due to the combination of ascending or descending cloud drops, raindrops, and graupel particles has the following form:

$$Q(z) = \frac{g}{c_p}\left[L_v\frac{\partial R^*_{cd}(z)}{\partial p} + L_v\frac{\partial R^*_{rd}(z)}{\partial p} + (L_v + L_f)\frac{\partial R^*_{ip}(z)}{\partial p}\right]. \tag{16}$$

A flow chart of the modified FSU algorithm is given in Fig. 5.

### c. Calibration correction for latent heat retrieval

Because the algorithm is uncalibrated with respect to any real-world reference, the retrieved daily latent heat profile can be assumed to contain a vertically distributed bias denoted by $\varepsilon(p)$. This represents the difference between the estimated and true daily net latent heating profiles for the AIP-3 area as a function of pressure. Note that $\varepsilon(p)$ can be expanded in a Fourier series over pressure range ($p_t$, $p_s$), representing the upper and lower levels of the atmosphere between which the heating takes place, that is, from the surface (denoted by *s*) to the tropopause (denoted by *t*):

$$\epsilon(p) \approx \frac{a_0}{2} + \sum_{n=1}^{\infty}\left[a_n\cos\frac{2n\pi p}{p_s - p_t} + b_n\sin\frac{2n\pi p}{p_s - p_t}\right], \tag{17}$$

where

Unauthenticated | Downloaded 12/05/23 04:44 PM UTC

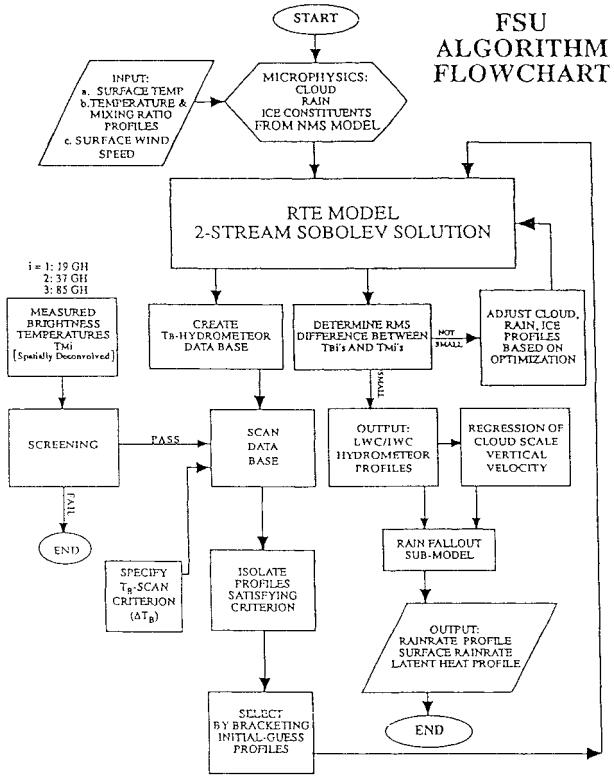


FIG. 5. Flowchart of new version of FSU rain profile retrieval algorithm.

$$a_n = \frac{2}{p_s - p_t}\int_{p_t}^{p_s} \epsilon(p)\cos\frac{2n\pi p}{p_s - p_t}dp \quad n = 0, 1, 2, \ldots, \quad (18)$$

$$b_n = \frac{2}{p_s - p_t}\int_{p_t}^{p_s} \epsilon(p)\sin\frac{2n\pi p}{p_s - p_t}dp \quad n = 1, 2, 3, \ldots. \quad (19)$$

If we select the first three harmonics as an approximation of the original profile, after rearrangement $\varepsilon(p)$ can be written as

$$\epsilon(p) \approx \frac{a_0}{2} + C_1 \cos\left[\frac{2\pi}{p_s - p_t}(p + C_2)\right], \quad (20)$$

where

$$a_0 = \frac{2}{p_s - p_t}\int_{p_t}^{p_s} \epsilon(p)\, dp. \quad (21)$$

In Eq. (20), $C_2$ is the initial phase, which determines the maximum amplitude ($C_1$) of the cosine function. From Eqs. (20) and (21) we know that the first term on the RHS of Eq. (20) is the vertically averaged bias. Therefore, the bias profile can be expressed by the sum of its mean and perturbation.

Since the vertical integration of the net condensation profile is equivalent to surface precipitation, we obtain

$$\langle L(\overline{c} - \overline{e}) + \epsilon\rangle = \mathrm{LP}, \quad (22)$$

where the averaging operator is expressed by

$$\langle\ \rangle = \frac{1}{g}\int_{p_t}^{p_s} (\ )\, dp. \quad (23)$$

Now $a_0$ can be estimated from Eqs. (20) and (21) by

$$a_0 = \frac{2g}{p_s - p_t}[\mathrm{LP} - \langle \mathrm{L}(\overline{c} - \overline{e})\rangle]. \quad (24)$$

At the tropopause level we assume no latent heating, thus the retrieved heating must also be zero. Assuming the bias $\varepsilon$ is zero at $p_t$, and using an optimization procedure to minimize the $\varepsilon(p)$ elements, we can solve for the two constants $C_1$ and $C_2$ to determine the mean bias profile. The optimization procedure consists of minimizing the integral differences between the retrieved and diagnosed latent heating profiles, cast as functions of height. This requires adjusting the $C_1$ and $C_2$ coefficients to achieve the smallest possible $\varepsilon(p)$ profile. If the resultant $\varepsilon(p)$ structure is nearly invariant with height, it means that the physics of the retrieval algorithm are reliable, insofar as vertical structure. We may thus conclude that the retrieved heating profiles are reliable if the magnitudes of the elements of $\varepsilon(p)$ are small and nearly invariant.

### *d. Diagnostic heat-moisture budgets over TOGA COARE IFA*

Averaging the thermodynamic energy and water vapor equations over a horizontal area yields the following expressions for $Q_1$ and $Q_2$ (e.g., Yanai et al. 1973):

$$Q_1 \equiv \frac{\partial \overline{s}}{\partial t} + \overline{\nabla \cdot s\mathbf{V}} + \frac{\partial \overline{s}\,\overline{\omega}}{\partial p}$$
$$= L(\overline{c} - \overline{e}) - \frac{\partial \overline{s'\omega'}}{\partial p} - Q_R \quad (25)$$

$$Q_2 \equiv -L\left(\frac{\partial \overline{q}}{\partial t} + \overline{\nabla \cdot q\mathbf{V}} + \frac{\partial \overline{q}\,\overline{\omega}}{\partial p}\right)$$
$$= L(\overline{c} - \overline{e}) + L\frac{\partial \overline{q'\omega'}}{\partial p}, \quad (26)$$

where $s = c_p T + gz$ is dry static energy, $T$ is temperature, $g$ is acceleration of gravity, $q$ is mixing ratio of water vapor, $\mathbf{V}$ is horizontal velocity, $\omega$ is vertical $p$-velocity, and $p$ is pressure. The overbar denotes an IFA horizontal average, $c$ is rate of condensation per unit mass of air, $e$ is rate of evaporation, and $Q_R$ is radiative cooling rate (which is available from published studies such as Dopplick 1972). The prime denotes the deviation from the average due to unresolved eddies stemming from cumulus convection and turbulence. The methods used for calculation of $Q_1$ and $Q_2$ are explained in appendix A.

Note that $Q_1$ consists of radiative cooling, net latent heat release, and vertical convergence of the vertical eddy transport of sensible heat, while $Q_2$ consists of net condensation and vertical divergence of the vertical

Unauthenticated | Downloaded 12/05/23 04:44 PM UTC

eddy transport of moisture. Comparing the vertical structures of $Q_1$ and $Q_2$ enables a determination of whether convection or stratiform systems are dominating. Similar vertical shapes of $Q_1$ and $Q_2$ would suggest stratiform systems while a vertical phase shift in the maximum levels of $Q_1$ and $Q_2$ would imply convectively driven precipitation.

After determining $Q_1$ and $Q_2$ from the large-scale diagnostic budget analysis and the latent heating retrieved from SSM/I measurements, the vertical eddy fluxes of sensible heat and moisture are obtained directly by residue based on Eqs. (25) and (26). These terms determine the contributions of unresolved eddies to $Q_1$ and $Q_2$, and are important quantities in understanding the role of cumulus convection on tropical energetics. The vertical eddy transports of moisture and the sensible heat are given by

$$L\frac{\partial\overline{q'\omega'}}{\partial p} = Q_2 - [L(\overline{c} - \overline{e}) + \epsilon], \tag{27}$$

$$-\frac{\partial\overline{s'\omega'}}{\partial p} = Q_1 - L(\overline{c} - \overline{e}) + Q_R. \tag{28}$$

To further check the validity of the diagnostic method, we can determine the bias between $\langle -\partial\overline{s'\omega'}/\partial p\rangle$ and the surface sensible heat flux ($S$), as well as the bias between $\langle L\partial\overline{q'\omega'}/\partial p\rangle$ and the surface latent heat flux (LE) by noting that the integrals of Eqs. (25) and (26) from tropopause ($p_t$) to surface ($p_s$) yield

$$\langle Q_1\rangle = \mathrm{LP} + S - \langle Q_R\rangle, \tag{29}$$

$$\langle Q_2\rangle = \mathrm{LP} - \mathrm{LE}, \tag{30}$$

where $P$, $S$, and $E$ are surface precipitation rate, sensible heat flux, and evaporation rate per unit area, respectively.

There are several methods that can be applied to determine the surface sensible heat and moisture fluxes. The bulk aerodynamic method is considered the most convenient because it only requires those meteorological parameters generally measured within a synoptic or climatological network. Although there is uncertainty in this method (e.g., Weare 1989), it is accurate enough to obtain reasonable estimates of the fluxes if the bulk transfer coefficients ($C_H$ and $C_E$) have been specified carefully (e.g., Cayan 1992). For this analysis, the validating surface fluxes are estimated from bulk transfer formulas given by

$$S = \rho c_p\overline{V}_s C_H(\overline{T}_s - \overline{T}_a), \tag{31}$$

$$\mathrm{LE} = \rho L\overline{V}_s C_E(\overline{q}_s - \overline{q}_a), \tag{32}$$

where the overbar has the same meaning as defined previously. The $\rho$ and $c_p$ quantities are density and isobaric specific heat of air, $L$ is latent heat of vaporization, $\overline{V}_s$ is mean surface wind speed, and $\overline{T}/\overline{q}$ are mean temperature and specific humidity of air at reference height and sea surface according to subscripts $a$ and $s$, respectively. The $C_H$ and $C_E$ factors are empirically defined bulk transfer coefficients, which are crucial to the method.

Bulk transfer formulas are generally not applicable under calm wind conditions. Therefore, we have selected constants for surface sensible and latent heat flux based on recent observations in the western Pacific ocean under low wind conditions (Bradley et al. 1991). Bulk transfer coefficients are complicated factors because they vary with the vertical gradient of wind speed, surface roughness, temperature, humidity, and drag coefficient, although they are often taken to be constant. Smith (1989) provided a careful review concerning measurement of evaporation. The study by Bradley et al. (1991) shows good agreement between bulk transfer coefficients derived from measurements, and those obtained from model runs and other observationally derived values under conditions of low surface wind speed. Because the environmental conditions for the study of Bradley et al. (1991) were similar to those of the TOGA COARE IFA, the $C_H$ and $C_E$ factors from that study have been selected for this analysis.

## 3. Description of datasets

The SSM/I instruments onboard the DMSP satellites have seven vertically (V) and horizontally (H) polarized channels (19V–H, 22V, 37V–H, 85V–H). The 85-GHz channels provide information about ice scattering above the freezing level, while the 19-GHz channels provide information about rain emission below the freezing level (Smith et al. 1992a; Mugnai et al. 1993). The 37-GHz channels provide a mixed set of information about scattering and emission from both liquid and frozen suspended and precipitating hydrometeors. SSM/I measurements from two satellites (F10 and F11) are used for this study. In addition, we use GMS satellite VIS and IR measurements and shipboard C-band radar measurements (all obtained from the TOGA COARE data archives) for the screening portion of the precipitation retrieval algorithm. Before the retrieval process is applied to the SSM/I measurements, the brightness temperatures at 19 and 37 GHz are spatially enhanced to the 13-km ground resolution of the 85-GHz channels in order to obtain spatial resolution consistency between different channels. This is mostly important for the radiative transfer calculations. An energy-conserving spatial deconvolution technique described by Farrar and Smith (1992) is used for this purpose; its impact on precipitation retrieval has been examined by Farrar et al. (1994).

The surface rain-rate validation data consist of maps of calibrated radar rain rates collected from two TOGA COARE shipboard Doppler radars (MIT and NOAA–TOGA) located at approximately 2°S–154.5°E and 2°S–156°E, as shown in Fig. 1. The maximum usable range of each radar is 145 km, yielding rain measurements in a circular region approximately 2.5° in diameter. In the

Unauthenticated | Downloaded 12/05/23 04:44 PM UTC

region of overlap between the two radar coverage zones, the maximum of two rain rates is selected for a given pixel position. Overall about one third of the 5° square AIP-3 region contained rain-rate signal according to the radars. The calibration of the radars is discussed in detail in Ferrier et al. (1999, manuscript submitted to *J. Atmos. Oceanic Technol.*). Radar reflectivities were measured every 10 min at a scan height of 2 km inside a range of 100 km. Beyond 100 km, the scan height increases from 2 to 3.8 km at 150-km range. A reflectivity threshold of 10 dB$Z$ was applied to the raw radar pixels to distinguish between raining and nonraining pixels (P. Kucera 1996, personal communication). All raining radar pixel reflectivities were converted to rain rates using $Z$–$R$ relationships $Z = 120R^{1.43}$ or $Z = 323R^{1.43}$ for convective rain and stratiform rain, respectively (see Ebert 1996). In order to reduce the effects of random error, the rain rates of raw radar measurements were then averaged over a $8 \times 8$ arrays to form 2-km grid cells. It was the gridded rain maps that were used in this study. Detailed descriptions of the TOGA COARE rain maps are discussed by Short et al. (1997).

The GMS measurements acquired for TOGA COARE were obtained through the AIP-3 project (Ebert 1996). The GMS subsatellite point is nominally 140°E. This satellite provides VIS/IR images every 30 min, which is the sampling time used for this study. No VIS imagery exists for the hours between 0730–1930 UTC.

The sounding dataset used in this study was derived from ISS measurements, which were taken four times a day at each of the eight TOGA COARE ISS sites. The instrumentation for an ISS includes a 915-MHz wind profiler, a Radio Acoustic Sounding System, an Omega-based NAVAID sounding system, and an enhanced surface meteorological station. The general philosophy behind the ISS is that the integration of various measurement systems overcomes each system's respective limitations, while taking advantage of its positive attributes (Parson et al. 1994). The ISS's can therefore provide high-quality datasets. The interpolated values at a constant pressure increment of 5 mb provided by the National Center for Atmospheric Research (NCAR) were used in this study.

In order to test the methodology, we sought the best possible sounding data time series to minimize problems with the $Q_1/Q_2$ calculations. Based on detailed visual analysis of the ISS dataset, there were relatively few missing data or bad data gaps in the sounding time series over the period 1–17 February 1993. The data recovery records of soundings, which bear out this analysis, can be found in the nine-volume technical report prepared by Miller (1994). Therefore, we have selected these 17 days as the ''best quality sounding period'' for purpose of analyzing the heating–moistening budgets over the IFA. The layer between 1000 and 100 mb was chosen as the vertical study range since many TOGA COARE soundings reached ~100 mb near the tropopause before losing signal. All missing data were first replaced using linear interpolation, then checked for vertical consistency. After applying a 25-mb running average to the high-resolution profiles, data points at 25-mb intervals were selected for the budget studies.

## 4. Algorithm validation over AIP-3 study area

Daily, instantaneous, and monthly timescales are considered for purposes of validation. The statistical analysis is conducted according to the procedures used for the GPCP satellite precipitation algorithm intercomparison projects referred to as AIP-1, AIP-2, and AIP-3; see Allam et al. (1993), Ebert (1996), and Ebert and Manton (1998). Rainfall validation data were obtained for the three TOGA COARE cruise periods based on the two IFA shipboard radar platforms located inside the 5° square AIP-3 study area (see Fig. 1). The periods of the three cruises were 1) 11 November–10 December 1992, 2) 15 December 1992–18 January 1993, and 3) 23 January–23 February 1993. These periods consisted of 30, 35, and 32 days, respectively.

The major statistical parameters incorporated in the validation include the sample size, the mean estimated and observed rain rates over the sample domain, the ratio of the two mean rain rates, the bias, the unadjusted rms error, and the correlation coefficient. The bias gives the actual rain-rate difference between the mean estimated and mean observed values, while their ratio is a simple measure of their relative magnitude. The correlation coefficient describes the ability of the algorithm to detect the spatial and temporal variations of rainfall in synchronization with the observed variations.

The observed and estimated daily rain rates are calculated on the basis of arithmetically averaging all 2-km radar and 13.5-km SSM/I pixels located in the radar coverage areas, for each day. Note that the frequency of radar reports is 10-min, while that of a single DMSP satellite is twice per day, meaning that the diurnal cycle of rainfall cannot be resolved by a single DMSP satellite. However, we estimate the main features of the diurnal cycle by including rain-rate estimates from two DMSP satellites (F10 and F11) at staggered orbit-crossing times. The relevant intercomparison statistics are given in Table 2a for individual cruises and all three cruises combined. It is evident that the relative magnitude for all-cruises combined is close to 1, with the ratios varying from 0.50 for cruise 1, to 1.18 for cruise 2, and 1.41 for cruise 3. The cruise-dependent bias factors vary from $-0.079$ to 0.058 mm h$^{-1}$, with the overall bias small (0.011 mm h$^{-1}$). The unadjusted rms factors range from 0.125 to 0.340 mm h$^{-1}$.

The comparison of daily rain-area coverage (fraction of raining pixels to total pixels) between the estimated and observed results is given in Table 2b in order to assess the reliability of the new FSU algorithm to estimate the spatial distribution of rainfall. It is evident that the estimated rain-area coverages are in good agreement with the radar, with relative magnitudes of 0.820,

Unauthenticated | Downloaded 12/05/23 04:44 PM UTC

TABLE 2a. Validation of daily mean rain rates over AIP-3 study area.

| Cruise No. | Number of Samples | Mean Obs (mm $h^{-1}$) | Mean Est (mm $h^{-1}$) | Ratio | Bias (mm $h^{-1}$) | rms (mm $h^{-1}$) | Correlation Coeff. |
|---|---|---|---|---|---|---|---|
| 1 | 30 | 0.156 | 0.077 | 0.496 | −0.079 | 0.125 | 0.800 |
| 2 | 35 | 0.247 | 0.291 | 1.179 | 0.044 | 0.340 | 0.778 |
| 3 | 32 | 0.140 | 0.198 | 1.414 | 0.058 | 0.258 | 0.719 |
| all | 97 | 0.183 | 0.194 | 1.058 | 0.011 | 0.262 | 0.743 |

TABLE 2b. Validation of daily rain-area coverages over AIP-3 study area.

| Cruise No. | Number of Samples | Mean Obs (%) | Mean Est (%) | Ratio | Bias (%) | rms (%) | Correlation Coeff. |
|---|---|---|---|---|---|---|---|
| 1 | 30 | 6.79 | 5.59 | 0.820 | −1.20 | 6.59 | 0.736 |
| 2 | 35 | 14.14 | 16.31 | 1.153 | 2.17 | 8.61 | 0.903 |
| 3 | 32 | 9.42 | 12.58 | 1.336 | 3.16 | 9.53 | 0.875 |
| all | 97 | 10.31 | 11.77 | 1.141 | 1.46 | 8.38 | 0.876 |

TABLE 2c. Validation of instantaneous rain rates over AIP-3 study area (overall).

| Cruise No. | Number of Samples | Mean Obs (mm $h^{-1}$) | Mean Est (mm $h^{-1}$) | Ratio | Bias (mm $h^{-1}$) | rms (mm $h^{-1}$) | Correlation Coeff. |
|---|---|---|---|---|---|---|---|
| 1 | 1152 | 0.124 | 0.070 | 0.546 | −0.054 | 0.256 | 0.777 |
| 2 | 1746 | 0.233 | 0.400 | 1.719 | 0.167 | 1.054 | 0.692 |
| 3 | 1580 | 0.171 | 0.215 | 1.263 | 0.045 | 0.555 | 0.673 |
| all | 4478 | 0.183 | 0.250 | 1.367 | 0.067 | 0.747 | 0.670 |

TABLE 2d. Validation of monthly rainfall over AIP-3 study area.

| Cruise No. | Number of Samples | Mean Obs (mm) | Mean Est (mm) | Ratio | Bias (mm) | rms (mm) | Correlation Coeff. |
|---|---|---|---|---|---|---|---|
| 1 | 26 | 92 | 45 | 0.49 | −47 | 53 | 0.31 |
| 2 | 25 | 193 | 266 | 1.38 | 73 | 115 | 0.24 |
| 3 | 26 | 115 | 157 | 1.38 | 43 | 71 | 0.67 |
| all | 77 | 133 | 155 | 1.17 | 22 | 84 | 0.71 |

1.153, 1.336, and 1.141 for cruises 1, 2, 3, and all-cruises combined. The maximum bias is 3.16%. The minimum and maximum correlation coefficients are 0.736 and 0.903.

The time series of estimated and observed daily rain rates and rain-area coverages are shown in Fig. 6. It is evident that the daily SSM/I-derived rain rates and rain-area coverages are generally consistent with the radar measurements. It should be pointed out that there is a tendency for the satellite to underestimate low rain rates and overestimate high rain rates with respect to the radar. The underestimation of light rain may be the result of shallow convective cells in light rain periods being too small to be fully resolved by the SSM/I beams, whereas the overestimation of heavy rain may be due to inadequacies in the cloud model. More importantly, the mismatch in diurnal sampling between the radar and satellite (on the order of 144 radar samples versus 4 SSM/I samples from two satellites) leads to incompatible differences. However, the lesson of the AIP-3 project was that the C-band radar estimates were also flawed (Short et al. 1997), so that the mean difference between the satellite estimates and the ground truth measurements cannot be taken as an absolute indicator of accuracy. By the same token, the mean difference can be used as a sanity check on the performance of both systems. In this case, it would appear that the satellite and radar estimates are within sufficient agreement to accept the satellite estimates as representative measures of rainfall over TOGA COARE, to within an uncertainty of less than 10% for the complete IOP.

The validation of instantaneous rain rates is based on averaged radar and SSM/I rain rates over 0.5° grid boxes. The 2 × 2 km resolution radar pixels are averaged onto the 0.5° grid palette. A radar grid is considered valid only if at least 30% of the radar pixels are reporting. This requirement eliminates most of the radar measurements at the periphery of the radar scans, which are also the least reliable because of propagation attenuation effects. Thus, only the most reliable radar rain rates are included in the validation process. The time difference tolerance between an SSM/I swath and a radar sweep is 10 min. The validation statistics for the three cruises are given in Table 2c. It can be seen that

Unauthenticated | Downloaded 12/05/23 04:44 PM UTC

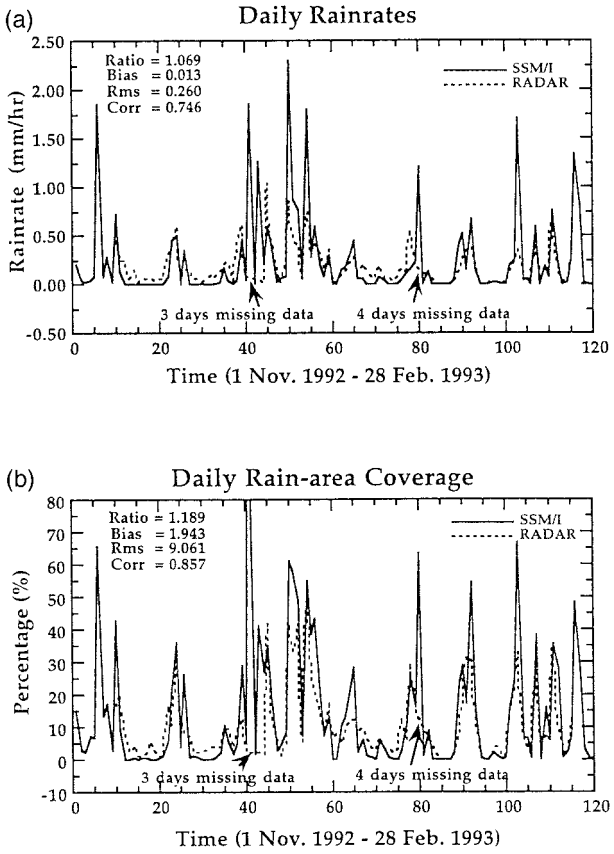


FIG. 6. Comparison of daily time series of SSM/I and radar derived rain rates (top panel) and rain-area coverage (bottom panel) for TOGA COARE intensive observational period.

rain rates are underestimated for cruise 1, and overestimated for cruises 2 and 3, as was found in the daily analysis. The greatest overestimate is for cruise 2, which was a period of enhanced convective activity within the TOGA COARE study area (McBride et al. 1995). Overall, the satellite estimates overestimate the radar observations by 37%. The ranges of bias, unadjusted rms, and correlation coefficient for the three cruises are $-0.054$ to 0.167 mm $h^{-1}$, 0.256 to 1.054 mm $h^{-1}$, and 0.673 to 0.788, respectively. Compared to results from the AIP-3 project (see Ebert 1996), the new version of the FSU algorithm performed better than 25, 20, and 12 of the 30 PMW algorithms participating in this project in conjunction with bias, rms error, and correlation coefficient, respectively.

In order to simplify the monthly rainfall analysis, total rainfall of each cruise is taken as ''monthly'' rainfall. A procedure described by Yang (1996) during the monthly rainfall accumulation process over a 0.5° grid resolution is made to ensure that all grid box values selected for the monthly validation are considered to be the most reliable data. The monthly statistical results are given in Table 2d. The show that overall, the SSM/I algorithm overestimates radar rainfall by 17%. Biases range from $-47$ to 73 mm for the individual cruises, with the maximum value corresponding to the most enhanced convection period (cruise 2). The overall bias is relatively small (22 mm) with a relative magnitude of 1.17. The correlation coefficients for the monthly results are small for cruises 1 and 2, although the coefficient reaches 0.67 for cruise 3, and its overall value is 0.71 when all cruises are combined.

In addition, case studies and the application of both binary (rain–no rain) and multiple-category contingency table analysis (similar to procedures used by Ebert 1996) were conducted to ascertain the consistency between the SSM/I rain-rate estimates and the radar measurements. The details of these comparisons are found in Yang (1996).

To test the significance of an estimated correlation coefficient from a finite data sample, the method described by Bendat and Piersol (1986) is used (summarized in appendix B). The results of the significance testing are given in Table 3. Although the values of estimated correlation coefficients vary considerably for different categories in the validation calculations because of the three different timescales, they are all significant at the 1% level except for monthly rainfall associated with cruises 1 and 2. For these two cases, in which the correlations coefficients drop to 0.31 and 0.24, the significance levels drop to 13% and 26%, respectively.

The validation analyses demonstrate the sensitivity of validation statistics to the analysis time scale and how the averaging is done. There are some notable differences on a cruise-by-cruise basis, although there is general consistency between the satellite estimates and the

TABLE 3. Significance of estimated correlation coefficients.

| | Daily mean rain rate | | Daily rain area coverage | | Instantaneous rain rate (all) | | Instantaneous rain rate (case) | | Monthly rainfall | |
|---|---|---|---|---|---|---|---|---|---|---|
| Cruise | Corr. | Signif. level (%) | Corr. | Signif. level (%) | Corr. | Signif. level (%) | Corr. | Signif. level (%) | Corr. | Signif. level (%) |
| 1 | 0.80 | 1 | 0.73 | 1 | 0.78 | 1 | 0.89 | 1 | 0.31 | 13 |
| 2 | 0.78 | 1 | 0.90 | 1 | 0.69 | 1 | 0.93 | 1 | 0.24 | 26 |
| 3 | 0.72 | 1 | 0.88 | 1 | 0.67 | 1 | 0.81 | 1 | 0.67 | 1 |
| all | 0.74 | 1 | 0.88 | 1 | 0.67 | 1 | 0.68 | 1 | 0.71 | 1 |

Unauthenticated | Downloaded 12/05/23 04:44 PM UTC

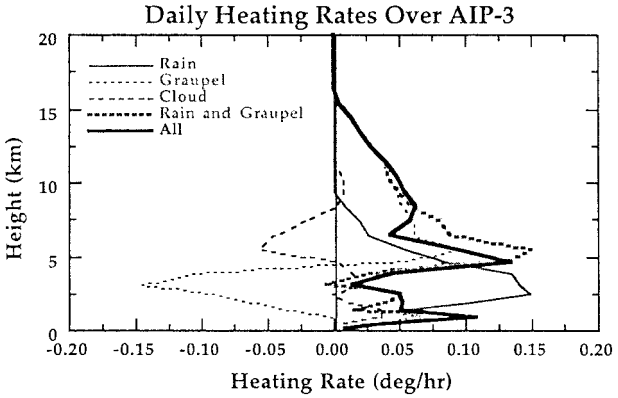


FIG. 7. All-cruise mean retrieved daily heating rates °C $hr^{-1}$ from SSM/I measurements over AIP-3 area due to rain, graupel, and cloud equivalent water contents using regressed cloud-scale vertical velocity in heating rate calculations. Rain + graupel and all-component profiles are also shown.

radar measurements and fairly close agreement between the two sets of data when considered in an all-cruise combined framework for daily and monthly timescales. In general, using the radar measurements as ground truth, the uncertainties in the satellite estimates for monthly, daily, and instantaneous rain rates are on the order of 17%, 6%, and 37%, respectively.

## 5. Moisture budget process in TOGA COARE IFA

### *a. Latent heating calibration*

Using the retrieved hydrometeor profiles from the new version of the FSU algorithm, latent heating profiles are obtained from Eq. (16). Heating rates are calculated on a pixel-by-pixel basis, then averaged spatially and temporally for different purposes. Only the effects of cloud, rain, and graupel are included in the heating process. The magnitude of total column heating due to cloud drop formation is relatively small compared to that due to precipitating rain and graupel. However, the vertical motion of cloud drops by the cloud-scale vertical velocity field can significantly modify the vertical structure of the heating profile. Figure 7 shows the component-wise, retrieved, daily averaged vertical heating rate structures for the three cruises over the AIP-3 study area. The condensation heat release due to raindrops is located in the lower troposphere with a maximum heating around 3 km. The heating in the middle–upper-troposphere is due primarily due to graupel deposition. The melting and evaporation of graupel particles are responsible for cooling below 5 km. The redistribution of cloud water due to cloud-scale vertical velocity results in enhanced heating below 5 km and reduced heating between 5 and 8.5 km. The salient characteristic of the retrieved total latent heating profile is that maximum heating is found at ~4.5 km. A secondary maximum is found at the 1-km level. These results suggest that the effect of cloud water condensation is to shift the maximum level of latent heating from 5.5 to 4.5 km, while reducing upper-level heating. A comparison of total latent heating due to rain and graupel with and without the cloud-scale vertical velocity adjustment leads to similar magnitudes; however, the vertical structure differences are significant enough to suggest that the impact of the cloud water storage term on the latent heat budget is important.

TABLE 4. Classification of daily mean rain-rate categories.

| Category | RR (mm $h^{-1}$) |
|---|---|
| 1 | $RR < 0.05$ |
| 2 | $0.05 \leq RR < 0.15$ |
| 3 | $0.15 \leq RR < 0.25$ |
| 4 | $0.25 \leq RR < 0.50$ |
| 5 | $0.50 \leq RR$ |

Applying the heating rate calibration scheme, the bias profiles are then calculated. Compared to the retrieved heating profile, the combined cruise averaged bias profile is relatively small, representing only 6% of the total retrieved heating. However, the bias profiles vary with retrieved rain rates, so these profiles are sorted into five categories based on a daily mean rain-rate classification given in Table 4. The averaged rain rates ($\overline{RR}_n$) for each category are 0.01, 0.09, 0.19, 0.38, and 0.99 mm $h^{-1}$, respectively. These categories correspond to trace, small, moderate, heavy, and intense rain rates, respectively. The mean retrieved rain-rate category-based heating profiles are shown in Fig. 8 (top panel) and as expected, the latent heating increases with rain rate. Figure 8 (bottom panel) shows the corresponding bias profiles. It is apparent that the magnitudes of the three negative bias and two positive bias profiles increase from rain-rate category 3 to 5 and from 1 to 2, respectively. The distribution of bias profiles can be explained by the fact that the FSU rain algorithm overestimates rain rates for heavy rainfall, and underestimates rain rates for light rainfall, relative to the radar data used to derived the biases. The largest bias comes from category 5 (intense) where the FSU algorithm makes the largest overestimates. Overall, the unweighted average (worst case) category bias is about 18% of the retrieved heating. This is to say that the original retrieved heating profile has 18% uncertainty if the underlying rain-rate frequency distribution is unknown.

The salient feature of the mean bias profiles is their discontinuous behavior with respect to rain rate. To obtain a semicontinuous bias adjustment profile for a given heating profile, the mean category-based bias profiles are scaled within their corresponding category according to surface rain rate. The actual heating adjustment for a daily averaged profile consists of two parts, a mean bias vector and a perturbation bias vector. The latter is proportional to the retrieved rain-rate deviation with respect to the category mean rain rate. Thus, a heating adjustment vector HA($z$) valid for all $z$ is given by

Unauthenticated | Downloaded 12/05/23 04:44 PM UTC

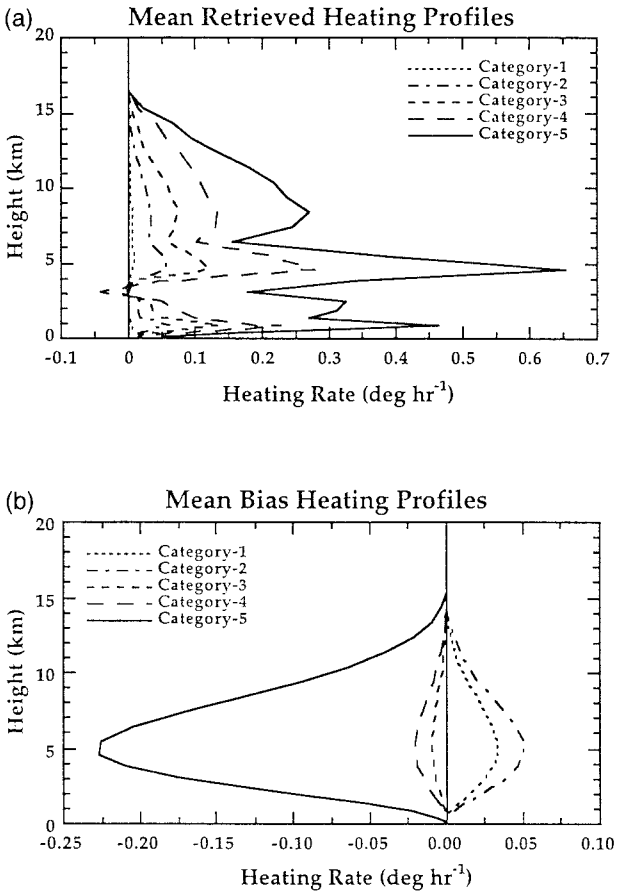


FIG. 8. Mean retrieved heating profiles (top panel) and associated bias profiles (bottom panel) for five different rain-rate categories over AIP-3 area.

$$\mathrm{HA}(z) = \mathrm{Bias}_n(z)\left(1 + \frac{(\mathrm{RR}_s - \overline{\mathrm{RR}}_n)}{\mathrm{Scale}_n}\right)$$
$$n = 1, 2, \ldots, 5, \qquad (33)$$

where $\mathrm{RR}_s$ is retrieved surface rain rate, $\overline{\mathrm{RR}}_n$ are category averaged rain rates, and $\mathrm{Scale}_n$ are associated with ranges of category intervals given by 0.05, 0.1, 0.1, 0.25, and 0.60 as $n$ changes from 1 to 5. When $\mathrm{RR}_s$ is assigned to the appropriate rain-rate category, the corresponding $\mathrm{Bias}_n$ vector, $\overline{\mathrm{RR}}_n$, and $\mathrm{Scale}_n$ used in Eq. (33) give the appropriate heating adjustment. This procedure was chosen over a continuous interpolation scheme to preserve the discontinuity produced by the algorithm's underestimation (overestimation) features for low (high) rain rates.

### *b. Latent heat estimates*

The new version of the FSU algorithm and the calibration scheme discussed above were applied to the TOGA COARE IFA for retrieval of latent heating profiles. Figure 9 (top panel) shows the averaged daily

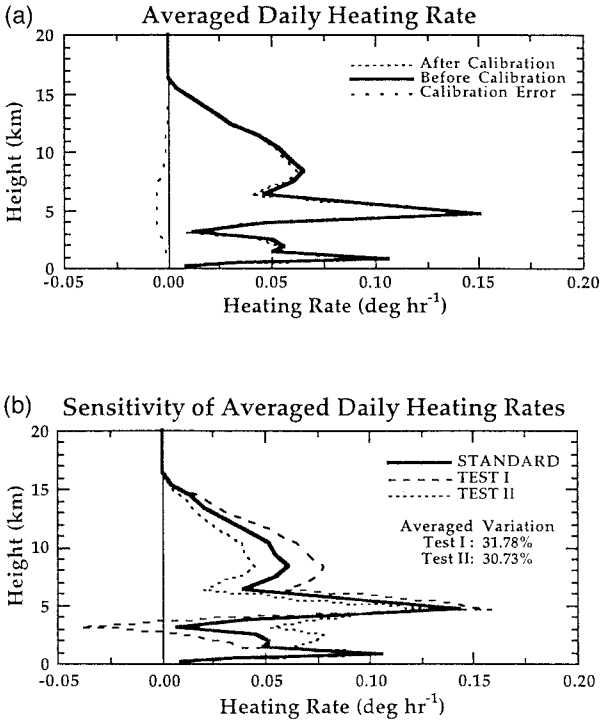


FIG. 9. Unadjusted and calibration-adjusted averaged daily latent heat profiles (°C $h^{-1}$) derived from SSM/I measurements over TOGA COARE IFA for Feb 1993 (top panel). Sensitivity tests of retrieved heating rate due to different ice densities and drag coefficients (bottom panel); standard, test I, and test II results are based on values of 600 kg $m^{-3}$ and 0.45, 900 kg $m^{-3}$ and 0.40, and 400 kg $m^{-3}$ and 0.60 for ice density and drag coefficient, respectively.

heating rate and its calibration over the IFA for February 1993. The monthly mean heating rate was obtained by averaging daily heating rates that were based on averaging all pixels falling within the IFA area on a given day from all swaths. The very small bias profile indicates that uncertainty in the initial retrieved heating profile is small for the IFA area on the monthly timescale. The maximum heating rate (3.6° $day^{-1}$) peaks around 4.5 km corresponding to a monthly mean rain rate of 0.21 mm $h^{-1}$. The two heating peak behavior is the result of a combination of convective and stratiform precipitation. The lower peak around 1 km is the result of precipitating convection modified by the vertical redistribution of cloud water due to the cloud-scale vertical velocity field.

Since the selection of ice density and drag coefficient involve uncertainties, sensitivity tests of the retrieved heating have been conducted for extreme combinations of ice density and drag coefficient. For test I, the ice density and drag coefficient are chosen as 900 kg $m^{-3}$ and 0.40, respectively. They are then set to 400 kg $m^{-3}$ and 0.60 for test II. The two test results are shown in Fig. 9 (bottom panel). The heating structures are similar although variations in magnitude up to 30% arise from varying these two factors.

Unauthenticated | Downloaded 12/05/23 04:44 PM UTC

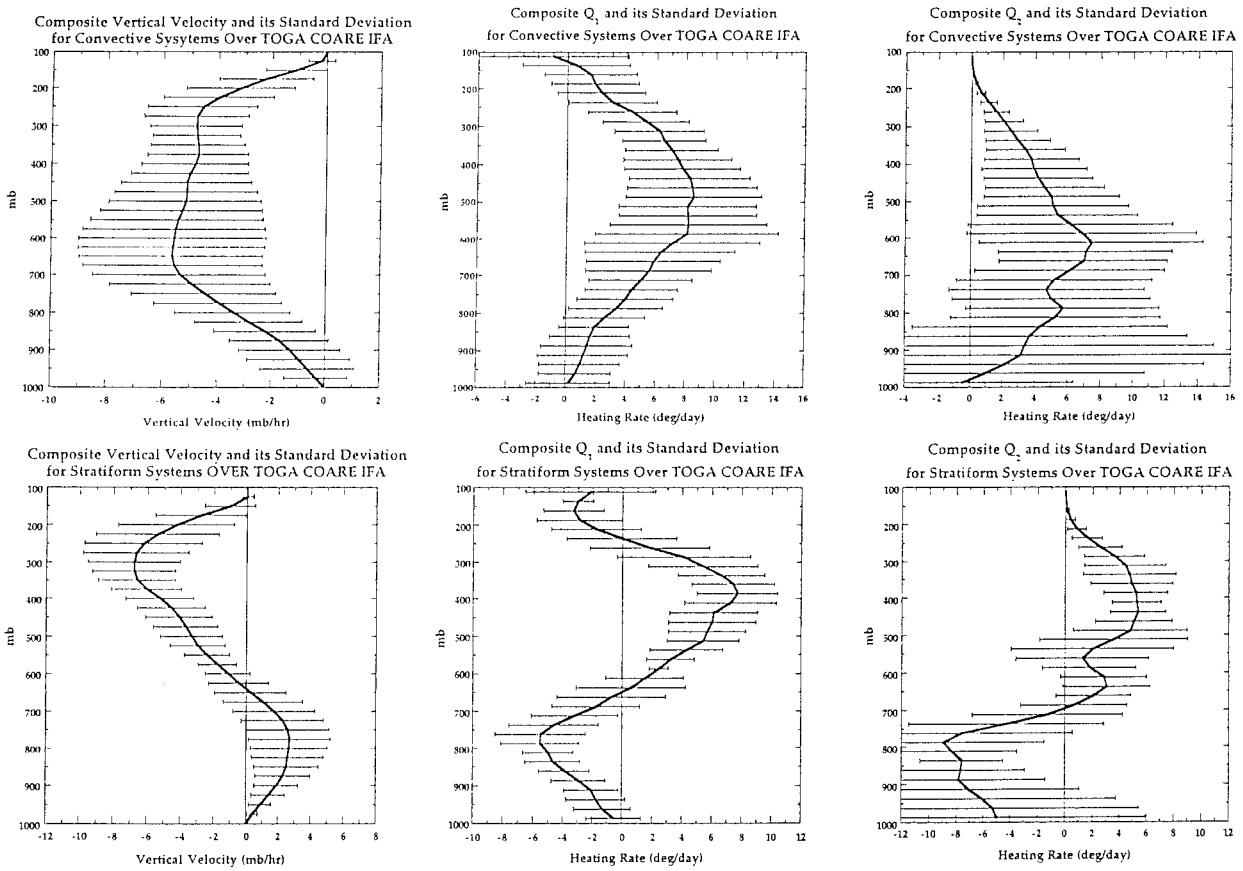


FIG. 10. Composite vertical structures of vertical velocity, $Q_1$, $Q_2$, and their standard deviations over TOGA COARE IFA. Top and bottom panels show profiles for convective and stratiform systems, respectively.

### *c. Moisture budget*

The optimal ISS sounding period of 1–17 February 1993 was selected for the large-scale $Q_1/Q_2$ budget analysis, with $Q_1/Q_2$ calculations made four times a day for the 17 days. The large-scale vertical velocity is mass-adjusted to force a zero-velocity boundary condition at 100 mb. An important feature of tropical cloud systems is that the vertical structures of $Q_1/Q_2$ for convective and stratiform systems are different. General tropospheric upward motion is associated with convective systems, while low-level tropospheric downward motion with rising motion above is indicative of stratiform systems (see Houze 1989).

Eight convective and four stratiform cases were chosen for composite analysis. The composite vertical velocity, $Q_1$, and $Q_2$ vertical distributions and their standard deviations are shown in Fig. 10. For the convective case, the vertical velocity is upward throughout the troposphere with a maximum of $-5.7$ mb h$^{-1}$ near 650 mb. Almost the entire troposphere is a positive heat source with maximum heating of $\sim 8.5°$ day$^{-1}$ around 500 mb. The moisture sink structure, which is similar to the Yanai et al. (1973) result, has two distinct peaks located at 600 and 775 mb, respectively. The maximum value of $Q_2$ is $\sim 7.4°$ day$^{-1}$. For stratiform systems, the vertical velocity field indicates sinking motion below 650 mb and rising motion above with maximum values of 2.7 mb h$^{-1}$ around 750 mb and $-6.8$ mb h$^{-1}$ around 300 mb. The main heat sink is below 650 mb with a secondary sink above 250 mb. The maximum heat source of 7.7° day$^{-1}$ is around 400 mb while the maximum heat sink of $-5.5°$ day$^{-1}$ is around 775 mb. The composite $Q_2$ profile shows an upper peak near 425 mb corresponding to 5.4° day$^{-1}$ equivalent drying, and a lower drying peak of 3.0° day$^{-1}$. These two peaks may be explained by variations in stratiform cloud bases. In addition, there is an equivalent $-9.0°$ day$^{-1}$ moistening rate near 775 mb. The moisture sink and source in the upper and lower troposphere are due primarily to condensation (plus deposition) and evaporation, respectively.

Notably, the $Q_1/Q_2$ profiles presented here are consistent with recently published TOGA COARE results (e.g., Lin and Johnson 1996; Frank and Wang 1996) as well as earlier results of Yanai et al. (1973) and Frank and McBride (1989). For example, the vertical structures and maximum values of $Q_1/Q_2$ are similar to those from Lin and Johnson (1996) over the TOGA COARE

Unauthenticated | Downloaded 12/05/23 04:44 PM UTC

study area, although they did not focus on convective and stratiform systems. Also, the shape and magnitude of our convective $Q_1$ structure is similar to that from Frank and Wang (1996) for situations of vertically integrated heating rate greater than 1.5°C day$^{-1}$. In a related paper (Yang and Smith 1999), we have conducted detailed heat-moisture budget comparisons over the complete IOP to many published $Q_1/Q_2$ results over different tropical convective and stratiform systems; these results also bear out the reliability of our calculations.

A comparison of composite $Q_1/Q_2$ profiles for convective systems shows that their peaks are located at different elevations, which is the basic signature for active cumulus convection. In contrast, the maxima of $Q_1/Q_2$ for stratiform systems are located at nearly equivalent altitudes, which shows why it is important to differentiate between the two cases. The standard deviation profiles for vertical velocity and $Q_1$ indicate that they are similar to the composite profiles. However, the large $Q_2$ standard deviations in the lower troposphere for stratiform systems and from low- to midtroposphere for convective systems show that moisture profiles are more irregular, especially at lower levels due to the greater variability of moisture distribution in convection areas as compared to dry static energy.

In order to quantify uncertainties in $Q_1$ and $Q_2$ caused by different methods of calculation, sensitivity tests were conducted by applying the second method described in appendix A. Instead of calculating the energy divergence terms in the $Q_1/Q_2$ equations, the second method calculates advection terms in an alternative set of equations. A comparison of two-day mean profiles for convective and stratiform systems is shown in Fig. 11. The $Q_1/Q_2$ profiles from the second method are given by diamonds and circles, respectively. The overall difference between the two methods is negligible, providing confidence in the diagnostic calculations.

Figure 12 presents the 17-day daily time series of $Q_1$, $Q_2$, and retrieved latent heating profiles over the TOGA COARE IFA. The retrieved surface rain rates are also shown in the bottom panel. Since the retrieved latent heating profiles must be consistent with surface rainfall, the degree of variability in the intensity of the heating must correspond to that of the surface rainfall. Notably, temporal variations in the diagnostic $Q_1$ and $Q_2$ profiles are consistent with those in the retrieved latent heating profiles. Thus it can be seen that the heating over the TOGA COARE IFA area mainly comes from latent heating.

Having the $Q_1$, $Q_2$, and latent heating profiles together, we can estimate the vertical eddy transports of sensible heat and moisture on the basis of Eqs. (27) and (28). Only the estimation of eddy moisture flux is discussed here because the estimates of eddy sensible heat flux would involve unknown errors due how the radiative cooling profile is specified. Figure 13 shows the eddy moisture flux profiles for two-day averaged convective and stratiform cases and for the 17-day mean. The four days chosen for the two composites were the best examples within the 17-day sequence of nearly pure-convective and pure-stratiform conditions. The relatively large magnitudes in the eddy moisture flux profiles indicate the importance of cumulus scale turbulence in tropical cloud systems. For the convective case, the effects of cumulus activity dry the low- to midtroposphere while moistening the upper troposphere. In contrast, the effects of turbulence for the stratiform case moistens the low and upper troposphere while mostly drying the midtroposphere. Comparison of the convective results to the Tao et al. (1993a) model results indicates structural agreement between the two sets of profiles. Comparison of the stratiform result to both their stratiform profiles are consistent in exhibiting low-level turbulent moistening capped by a shallow layer of drying and the mid- to upper-level drying–moistening oscillation. There is no similar profile in the Tao et al. study to our 17-day all-weather result, which shows general eddy flux moistening except near 3 km.

Since the vertical integral of the eddy moisture flux is equivalent to the surface latent heat flux, we can

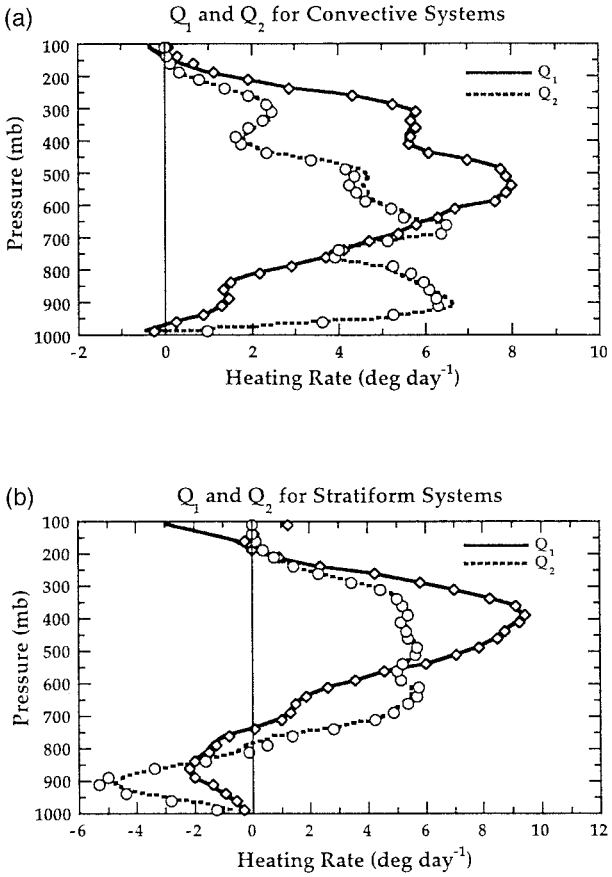


FIG. 11. Sensitivity test of diagnostic method based on two-day averaged $Q_1$ and $Q_2$ profiles over TOGA COARE IFA for convective (top panel) and stratiform systems (bottom panel). Diamonds and circles present $Q_1$ and $Q_2$ from second method of calculation.

Unauthenticated | Downloaded 12/05/23 04:44 PM UTC

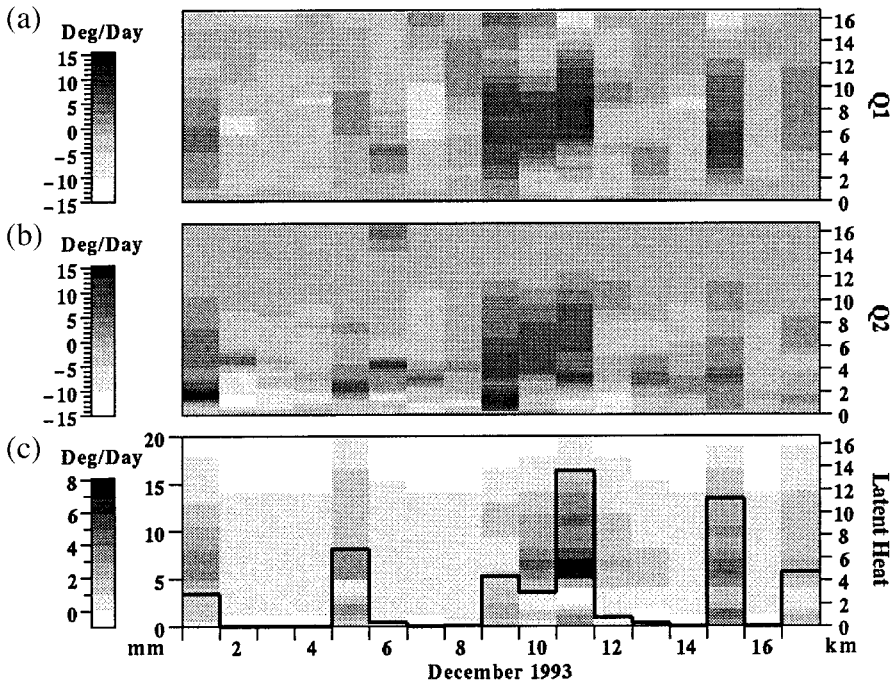


FIG. 12. Time series of daily mean $Q_1$ (top panel), $Q_2$ (middle panel), and latent heating (bottom panel) profiles over TOGA COARE IFA for 1–17 Feb 1993. Here, $Q_1$ and $Q_2$ are calculated from large-scale ISS sounding data. Latent heating is retrieved from SSM/I measurements based on new version of FSU precipitation retrieval algorithm.

determine the overall uncertainty in the eddy moisture flux profile by comparing the estimated and measured daily evaporation. The measured evaporation is calculated from the bulk formula given in Eq. (32) and with near-surface winds and specific humidity taken from the ISS soundings (sea surface saturation specific humidities are calculated at SST values obtained from the ship network). A value of $1.2 \times 10^{-3}$ was selected for the moisture bulk transfer coefficient from Bradley et al. (1991). Figure 14 is the comparison of estimated and measured daily evaporation over the 1–17 February period. Our averaged estimate (3.71 mm day$^{-1}$) over this period is very close to the results (3.7 mm day$^{-1}$) from TOGA COARE buoy data over the entire IOP (Lin and

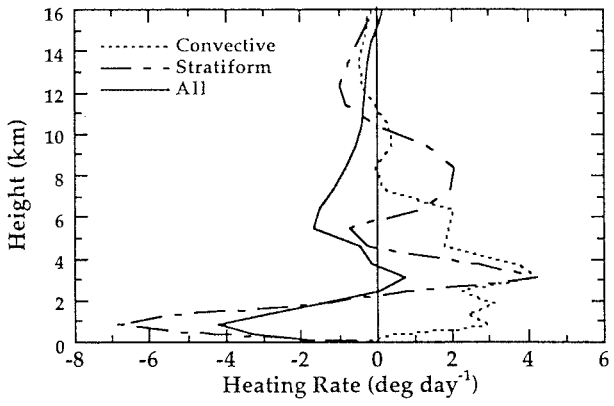


FIG. 13. Estimated eddy moisture flux profiles of two-day averaged convective and stratiform cases and all-day average over TOGA COARE IFA. Solid line is 17-day average result; two-day convective and stratiform averages are based on 9–15 Feb and 10–11 Feb, respectively.

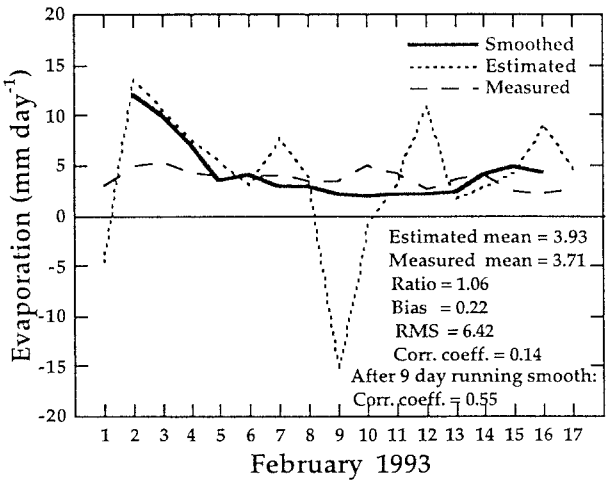


FIG. 14. Comparison of measured and satellite-estimated surface evaporation over TOGA COARE IFA area during 1–17 Feb 1993. Measured evaporation is calculated from bulk formula. Key statistical parameters are given in lower-right corner. Bold line is a nine-day smoothed rendition of satellite estimate based on extended time series from 31 Jan to 18 Feb.

Unauthenticated | Downloaded 12/05/23 04:44 PM UTC

Johnson 1996). Further comparison of our results to the buoy data over the same period indicates that our value is about 5%–10% smaller.

It is worth noting that in a recent paper by Fairall et al. (1996), they developed a more refined bulk parameterization of air–sea fluxes based on TOGA COARE buoy data. In addition to an equation similar to (32) used for latent heat calculation, they introduced two more parameters involving stability and gustiness that are relevant to surface-layer and boundary layer flux processes. For very weak wind situations, including these two parameters in their parameterization led to a combined enhancement of fluxes by about a factor of 4. However, since very small wind speeds during the IOP were a rare occurrence, the overall effect of the new parameterization on flux enhancement was only ~30% for surface wind speeds above 1 m $s^{-1}$. A comparison of our surface evaporation calculations using Eq. (32) to those from Fairall et al.'s method indicates that our results are 10% smaller.

It must be expected that the estimated daily evaporation rates are noisy due to using a residual approach between two independent sets of calculations, each with their own distinct uncertainties. In addition, some of the values are nonphysical (negative), that is, an outcome of the intrinsic noise properties as opposed to a problem with the basic approach. The noise in the daily estimates gives rise to poor correlation with the measurements. However, as evident from Fig. 14, the 17-day means are nearly the same (within 6%). Even with 10% adjustment to the measured evaporation, the estimated value using satellite measurements is still close to the measured value. This suggests that although the estimated daily evaporation contains an expected degree of uncertainty, averaging can reduce the associated errors to acceptable levels. For example, the correlation coefficient rises to 0.55 when a nine-day running average is applied. This suggests that by combining SSM/I and sounding measurements, it is possible to estimate the averaged eddy moisture flux profiles over designated space and time scales.

## 6. Discussion and conclusions

Various new modifications to the FSU rain profile algorithm have been implemented and investigated. A new precipitation screening scheme was developed on the basis of GMS VIS–IR, C-band radar, and SSM/I measurements. The GMS and radar measurements were used to identify clear and raining SSM/I pixels, respectively. A scattering index and three rain indices were then developed from the associated SSM/I brightness temperatures to distinguish between clear, nonraining cloud, and raining SSM/I pixels. Consideration of the effects of sea surface roughness and foam on surface emissivity was found to improve the characterization of the ocean boundary in radiative transfer calculations. Such improvements are significant in modeling upwelling $T_B$'s, particularly for clear sky and at low frequencies for nonraining cloud.

A semiempirical scheme was developed to estimate cloud-scale vertical velocity from a numerical simulation of an evolving tropical storm produced by the UW–NMS model. The prognosed hydrometeor LWCs–IWCs and vertical velocities were used in a multiregression analysis to enable diagnosing cloud-scale vertical velocity profiles. The resulting uncertainties were small enough to warrant using this method in the retrieval algorithm to adjust the precipitation fallout rates calculated after the hydrometeor profiles are determined. Using this scheme, the effects of cloud-scale vertical velocity on both rain rates and latent heating profiles have been examined. The modification is designed to account for more physical processes relevant to the estimation of latent heating.

Validation studies were conducted to demonstrate the soundness of the new version of the algorithm and to determine uncertainty relative to TOGA COARE C-band radar retrievals of rain rate, recognizing that such data are by themselves imperfect and should not be used as a final measure of accuracy or precision. The validation analyses were conducted over the AIP-3 study area. Intercomparison of daily mean rain rates over the entire TOGA COARE IOP result in a small bias of $+0.011$ mm $h^{-1}$ (a 6% overestimate relative to the radar mean) and a 0.74 correlation indicating that the estimated satellite rain rates are generally consistent with the radar rain rates in terms of magnitude and time variability. The rain-area coverage intercomparison of the daily mean results also produces a small bias of 1.1% (a 14% overestimate relative to the radar mean) and a 0.88 correlation. These results suggest that the new SSM/I screening scheme is reliable. The intercomparison involving instantaneous rain rates indicates the algorithm overestimates magnitudes by ~37% with moderately high correlation (0.67).

Overestimation is the expected result based on the findings of the AIP-3 intercomparison project in which 23 of the 27 passive microwave algorithms overestimated the shipboard radar data on a monthly basis by relative bias factors of just over 1.0 up to a factor of 3.45; see Ebert (1996) and Ebert and Manton (1998). Monthly rainfall derived from satellite measurements is one of the more important parameters in global climate studies. Here, the total rainfall amounts for each TOGA COARE cruise were taken to represent monthly rainfall. Overall, the new version of the FSU algorithm indicates 17% overestimation with respect to the TOGA COARE ship radar with an overall correlation coefficient of 0.71. Again, the overestimation is consistent with what was found in the AIP-3 study, although smaller than the 27-algorithm average overestimation of 48% and associated medium of 30%.

Analysis of latent heat retrievals was also conducted over the AIP-3 study area. Besides the heating due to precipitating rain and ice, it was also possible to con-

Unauthenticated | Downloaded 12/05/23 04:44 PM UTC

sider the heating effects of suspended cloud water through introduction of cloud-scale vertical velocity. Although this quantity does not contribute significantly to net heating, it does adjust the structure of the vertical heating profile such that the three-cruise averaged level of maximum heating is shifted downward from 5.5- to 4.5-km altitude. A latent heat calibration scheme was developed based on the requirement that vertical integration of the retrieved latent heating must equal the heating released from surface precipitation as estimated from the shipboard radar. This results in an approximately 6% upward bias adjustment to the retrieved latent heating taken with respect to the three-cruise average. The calibration adjustments were incorporated as a function of retrieved rain rate to account for algorithm underestimation at the light end of the scale and overestimation at the heavy end of the scale, again with respect to the ship radar. Applying the algorithm and the heating calibration scheme to the TOGA COARE IFA area, we obtained latent heating profiles over the region in which we could derive $Q_1/Q_2$ budgets. All-cruise composite profiles of the separate heating components due to precipitating rain, ice, their combination, cloud alone, and all terms were thus calculated over the IFA (Fig. 7).

A 17-day high quality ISS dataset (1–17 February 1993) was used to study the complete heat-moisture budgets. The derived composite $Q_1/Q_2$ structures for convection and stratiform systems are consistent with previous studies. For convective systems, $Q_1$ has a maximum heating rate of 8.5° day$^{-1}$ near 500 mb, whereas $Q_2$ has an upper peak of 7.4° day$^{-1}$ near 600 mb and a lower peak of 5.7° day$^{-1}$ around 775 mb. For stratiform systems, $Q_1$ has an upper peak of 7.7° day$^{-1}$ near 400 mb and a lower peak of $-5.5°$ day$^{-1}$ around 775 mb, whereas $Q_2$ has an upper peak of 5.4° day$^{-1}$ near 425 mb and a lower peak of $-9.0°$ day$^{-1}$ near 775 mb.

Further analysis of the $Q_2$ budget was conducted using the retrieved latent heating from SSM/I, in which the residual between $Q_2$ and the latent heating is a measure of the eddy moisture flux divergence due to convective-scale turbulence. Our foremost objective here has been to examine the vertical structure of turbulent-driven moisture fluxes for convective and stratiform environments, terms which are not yet fully understood in the context of the atmospheric moisture budget. In order to demonstrate the credibility of the residual calculations, we compared independent estimates of surface evaporation rates based on the bulk aerodynamic method to the integrals of the residual eddy moisture flux profiles, which are equivalent to the surface moisture fluxes (i.e., evaporation rates). This intercomparison was noisy on a daily basis but indicated a relatively small bias over the 17-day period. Therefore, the composite results we present in Fig. 13 concerning estimates of turbulent driven moistening and drying of the lower, middle, and upper layers of convective and stratiform systems, although containing uncertainty, appear to be reliable. The structural behavior of both convective and stratiform eddy flux moisture profiles are consistent with synonymous cases from the Tao et al. (1993a) study.

Clearly a 17-day sample is insufficient to make firm conclusions, suggesting that further analysis of the procedure would be worthwhile. Therefore, similar calculations are currently underway for the entire IOP. Notably, we can obtain the eddy sensible heat flux in the same fashion as the eddy moisture flux given reasonable estimates of the radiative flux divergence profile. With adequate refinement, such a diagnostic scheme within an observational framework could help in the development of parameterizations of turbulent-driven heat and moisture flux processes in precipitating cloud systems. This would lead to a better understanding of the contributions by turbulent transports to the total heating-moistening process. Further refinement might enable retrievals of the complete heat-moisture structures from SSM/I or SSM/I-like algorithms being developed for the TRMM measurements. This would be a useful development for improving physical parameterization schemes used in numerical prediction models.

*Acknowledgments.* The authors appreciate the assistance of Dr. Xuwu Xiang in implementing the FSU profile retrieval algorithm for this research. The authors also wish to thank Dr. Elizabeth Ebert for her assistance and cooperation in conducting the rain-rate validation, and Mr. Jim Merritt for his capable assistance in providing computational support. This research has been supported by NSF Grant ATM-9300870 and NASA Grant NAGW-3970. A portion of the computing resources has been provided by the Supercomputer Computation Research Institute at The Florida State University under U.S. Department of Energy Contract DOE-FC05-85ER250000.

## APPENDIX A

### Calculation of $Q_1-Q_2$ Quantities

Since the shape of the TOGA COARE IFA area is irregular, we calculate the area-averaged divergence related quantities by applying Green's theorem so that the areal integral is converted into integration along the periphery of the IFA boundaries (whose area is denoted by A). The following equations are then used for calculation of the $Q_1$ and $Q_2$ terms as given in Eqs. (25) and (26) of section 2d (see Yanai et al. 1973):

$$A = \frac{1}{2}\int (x\,dy - y\,dx), \tag{A1}$$

$$\overline{\nabla \cdot \mathbf{V}} = \frac{1}{A}\int (u\,dy - v\,dx), \tag{A2}$$

$$\overline{\nabla \cdot s\mathbf{V}} = \frac{1}{A}\int (su\,dy - sv\,dx), \tag{A3}$$

$$\overline{\nabla \cdot q\mathbf{V}} = \frac{1}{A}\int (qu\,dy - qv\,dx). \tag{A4}$$

Unauthenticated | Downloaded 12/05/23 04:44 PM UTC

The averaged vertical $p$-velocity is obtained by

$$\overline{\omega} = \int_{p_0}^{p} - \overline{\nabla \cdot \mathbf{V}}\, dp, \tag{A5}$$

where $p_0$ is set to 1000 mb, and vertical velocity is set to zero at both 100 and 1000 mb.

To start the calculations, eight ISS soundings were interpolated into 0.1° gridded latitude–longitude datasets by applying the NCAR interpolation scheme. Calculations are made at 25-mb intervals from 1000 to 100 mb. The initial estimates of divergence and vertical velocity are mass adjusted so that vertical velocity properly vanishes at 100 mb.

To make corrections for the budget quantities $\overline{\nabla \cdot s\mathbf{V}}$ and $\overline{\nabla \cdot q\mathbf{V}}$, we assume that each horizontal flux divergence quantity consists of both mean and eddy transport terms due to horizontal asymmetries, that is,

$$\overline{\nabla \cdot s\mathbf{V}} = \overline{s\nabla \cdot \mathbf{V}} + \text{eddy}, \tag{A6}$$

where $\overline{s}$ is the area averaged static energy over the IFA region. Assuming the correction to $\overline{\nabla \cdot s\mathbf{V}}$ does not affect the eddy component, we obtain

$$\begin{aligned}\overline{\nabla \cdot s\mathbf{V}}_{\text{cor}} &= \overline{s}(\overline{\nabla \cdot \mathbf{V}} + \overline{\nabla \cdot \mathbf{V}}_{\text{adj}}) + \text{eddy} \\ &= \overline{\nabla \cdot s\mathbf{V}} + \overline{s}\overline{\nabla \cdot \mathbf{V}}_{\text{adj}},\end{aligned} \tag{A7}$$

where $\overline{\nabla \cdot \mathbf{V}}_{\text{adj}}$ is the mass-adjusted correction of $\overline{\nabla \cdot \mathbf{V}}$. Similarly, we can correct to $\overline{\nabla \cdot q\mathbf{V}}$. All values of $\overline{\nabla \cdot \mathbf{V}}$, $\overline{\nabla \cdot s\mathbf{V}}$, and $\overline{\nabla \cdot q\mathbf{V}}$ are corrected before using them in the $Q_1$ and $Q_2$ equations.

As a sensitivity test, a second method of calculating $Q_1$ and $Q_2$ is compared to the first method. The second method is given by (see Keenan and Carbone 1992)

$$Q_1 = \frac{\partial \overline{s}}{\partial t} + \overline{\mathbf{V}} \cdot \nabla \overline{s} + \overline{\omega}\frac{\partial \overline{s}}{\partial p}, \tag{A8}$$

$$Q_2 = -L\left(\frac{\partial \overline{q}}{\partial t} + \overline{\mathbf{V}} \cdot \nabla \overline{q} + \overline{\omega}\frac{\partial \overline{q}}{\partial p}\right). \tag{A9}$$

The basic difference between the two methods is that the first is formulated in terms of the divergence of energy flux, whereas the second is formulated in terms of the advection of energy, although they are equivalent calculations vis-a-vis the continuity equation. Each of the methods has been employed in past studies. The two methods will exhibit varying sensitivity to uncertainties in the input data. Test results discussed in section 5c indicate that the budget calculations over the IFA using the ISS data are not sensitive to which method is employed.

## APPENDIX B

### Significance of Estimated Correlation Coefficient

Because of the variability of correlation estimation induced by finite sample sizes, it is usually desirable to verify that a nonzero value of a sample correlation coefficient reflects the existence of a statistically significant correlation between the variables of interest. The method of analysis for determining the reliability of an estimated correlation coefficient can be found in the text of Bendat and Piersol (1986). To evaluate the accuracy of a given correlation estimate $r_{xy}$ between random variables $x$ and $y$, it is convenient to work with a particular function of $r_{xy}$ given by

$$w = \frac{1}{2}\ln\left[\frac{1 + r_{xy}}{1 - r_{xy}}\right]. \tag{B1}$$

The random variable w has an approximately normal distribution with mean-variance:

$$\mu_w = \frac{1}{2}\ln\left[\frac{1 + \rho_{xy}}{1 - \rho_{xy}}\right] \qquad \sigma_w^2 = \frac{1}{N - 3}, \tag{B2}$$

where $r_{xy}$ is the true correlation between $x$ and $y$, and $N$ is the available sample size from which $r_{xy}$ must be estimated.

Using the above relationships, a confidence interval for $r_{xy}$, based on a sample estimate $r_{xy}$, may be established. This can be done by testing the hypothesis that $r_{xy} = 0$, where a significant correlation is indicated if the hypothesis is rejected. From Eq. (B2), the sample distribution of $w$, for an $N$-sized sample given that $r_{xy}$ is 0, would be normal with $m_w = 0$ and $\sigma_w^2 = 1/(N - 3)$. The acceptance region for the hypothesis of zero correlation is then given by

$$-z_{\alpha/2} \le z < z_{\alpha/2}, \tag{B3}$$

where $z$ is the standardized normal variable

$$z = \frac{\sqrt{N - 3}}{2}\ln\left[\frac{1 + r_{xy}}{1 - r_{xy}}\right], \tag{B5}$$

and $z_{\alpha/2}$ defines the level of significance. Values outside the above interval constitute evidence of statistical correlation at a level of significance dictated by the magnitude of $z_{\alpha/2}$. For example, absolute values of $z$ greater than 1.96 or 2.58 would indicate that the estimated correlation coefficients are significant at the 5% or 1% levels, respectively.

## REFERENCES

Adler, R. F., A. J. Negri, P. R. Keehn, and I. M. Hakkarinen, 1993: Estimation of monthly rainfall over Japan and surrounding waters from a combination of low-orbit microwave and geosynchronous IR data. *J. Appl. Meteor.*, **32,** 335–356.

Allam, R., G. Holpin, P. Jackson, and G.-L. Liberti, 1993: Second Algorithm Intercomparison Project of the Global Precipitation Climatology Project (AIP-2). Pre-Workshop Report, Satellite Image Applications Group, United Kingdom Meteorological Office, 439 pp. [Available from Satellite Image Applications Group, United Kingdom Meteorological Office, Bracknell, Berkshire RG12 2SZ, United Kingdom.]

Aonashi, K., A. Shibata, and G. Liu, 1996: An over-ocean precipitation retrieval using SSM/I multichannel brightness temperatures. *J. Meteor. Soc. Japan,* **74,** 617–637.

Arkin, P. A., and P. Xie, 1994: The Global Precipitation Climatology

Unauthenticated | Downloaded 12/05/23 04:44 PM UTC

Project: First Algorithm Intercomparison Project. *Bull. Amer. Meteor. Soc.,* **75,** 401–419.
Barrett, E. C., and Coauthors, 1994: The First WetNet Precipitation Intercomparison Project (PIP-1): Interpretation of results. *Remote Sens. Rev.,* **11,** 303–373.
Bauer, P., and P. Schluessel, 1993: Rainfall, total water, ice water, and water vapor over sea from polarized microwave simulations and Special Sensor Microwave/Imager data. *J. Geophys. Res.,* **98,** 20 737–20 759.
Bendat, J. S., and A. G. Piersol, 1986: *Random Data: Analysis and Measurement Procedures.* 2d ed. Wiley-Interscience, 566 pp.
Berg, W., and R. Chase, 1992: Determination of mean rainfall from the Special Sensor Microwave/Imager (SSM/I) using a mixed lognormal distribution. *J. Atmos. Oceanic Technol.,* **9,** 129–141.
Bradley, E. F., P. A. Coppin, and J. S. Godfrey, 1991: Measurements of sensible and latent heat flux in the western equatorial Pacific Ocean. *J. Geophys. Res.,* **96,** 3375–3389.
Cayan, D. R., 1992: Latent and sensible heat flux anomalies over the northern oceans: Driving the sea surface temperature. *J. Phys. Oceanogr.,* **22,** 859–881.
Chang, S. W., and T. R. Holt, 1994: Impact of assimilating SSM/I rainfall rates on numerical prediction of winter cyclones. *Mon. Wea. Rev.,* **122,** 151–164.
Cornejo-Garrido, A. G., and P. H. Stone, 1977: On the heat balance of the Walker circulation. *J. Atmos. Sci.,* **34,** 1155–1162.
Dopplick, T. G., 1972: Radiative heating of the global atmosphere. *J. Atmos. Sci.,* **29,** 1278–1294.
Ebert, E. E., 1996: Results of the 3d Algorithm Intercomparison Project (AIP-3) of the Global Precipitation Climatology Project (GPCP). BMRC Research Rep. 55, Bureau of Meteorology Research Centre, Melbourne, Australia, 199 pp. [Available from Bureau of Meteorology Research Centre, GPO Box 1289K, Melbourne, 3000 Australia.]
——, and M. J. Manton, 1998: Performance of satellite rainfall estimation algorithms during TOGA COARE. *J. Atmos. Sci.,* **55,** 1537–1557.
Fairall, C. W., E. F. Bradley, D. P. Rogers, J. B. Edson, and G. S. Young, 1996: Bulk parameterization of air–sea fluxes from Tropical Ocean-Global Atmosphere Coupled-Ocean Atmosphere Response Experiment. *J. Geophys. Res.,* **101,** 3747–3764.
Farrar, M. R., and E. A. Smith, 1992: Spatial resolution enhancement of terrestrial features using deconvolved SSM/I microwave brightness temperatures. *IEEE Trans. Geosci. Remote Sens.,* **30,** 349–355.
——, ——, and X. Xiang, 1994: The impact of spatial resolution enhancement of SSM/I microwave brightness temperatures on rainfall retrieval algorithms. *J. Appl. Meteor.,* **33,** 313–333.
Ferraro, R. R., and G. F. Marks, 1995: The development of SSM/I rain rate retrieval algorithms using ground-based radar measurements. *J. Atmos. Oceanic Technol.,* **12,** 755–770.
——, F. Weng, N. C. Grody, and A. Basist, 1996: An eight-year (1987–1994) time series of rainfall, clouds, water vapor, snow cover, and sea ice derived from SSM/I measurements. *Bull. Amer. Meteor. Soc.,* **77,** 891–905.
Ferrier, B. S., J. Gerlach, P. Kucera, D. Short, S. Rutledge, J. Lutz, and O. Thiele, 1999: Corrections and comparisons of TOGA COARE shipborne radar reflectivities. *J. Atmos. Oceanic Technol.,* in press.
Frank, W. M., and J. L. McBride, 1989: The vertical distribution of heating in AMEX and GATE cloud clusters. *J. Atmos. Sci.,* **46,** 3464–3478.
——, and H. Wang, 1996: Rawinsonde budget analyses during the TOGA COARE. *J. Atmos. Sci.,* **53,** 1761–1780.
Gill, P. E., W. Murray, and M. H. Wright, 1981: *Practical Optimization.* Academic Press, 401 pp.
Grody, N. C., 1991: Classification of snow cover and precipitation using the Special Sensor Microwave Imager. *J. Geophys. Res.,* **96,** 7423–7435.
Hack, J. J., and W. H. Schubert, 1990: Some dynamical properties of idealized thermally-forced meridional circulations in the tropics. *Meteor. Atmos. Phys.,* **44,** 101–118.
——, ——, D. E. Stevens, and H.-C. Kuo, 1989: Response of the Hadley circulation to convective forcing in the ITCZ. *J. Atmos. Sci.,* **46,** 2957–2973.
Hartmann, D. L., H. H. Hendon, and R. A. Houze Jr., 1984: Some implications of the mesoscale circulations in tropical cloud clusters for larger-scale dynamics and climate. *J. Atmos. Sci.,* **41,** 113–121.
Houze, R. A., Jr., 1982: Cloud clusters and large-scale vertical motions in the Tropics. *J. Meteor. Soc. Japan,* **60,** 396–410.
——, 1989: Observed structure of mesoscale convective systems and implications for large-scale heating. *Quart. J. Roy. Meteor. Soc.,* **115,** 427–461.
——, 1997: Stratiform precipitation in regions of convection: A meteorological paradox? *Bull. Amer. Meteor. Soc.,* **78,** 2179–2196.
Janowiak, J. E., 1992: Tropical rainfall: A comparison of satellite-derived rainfall estimates with model precipitation forecasts, climatologies, and observations. *Mon. Wea. Rev.,* **120,** 448–462.
Johnson, R. H., 1984: Partitioning tropical heat and moisture budgets into cumulus and mesoscale components: Implications for cumulus parameterization. *Mon. Wea. Rev.,* **112,** 1590–1600.
Keenan, T., and R. E. Carbone, 1992: A preliminary morphology of convective storms in tropical northern Australia. *Quart. J. Roy. Meteor. Soc.,* **118,** 283–326.
Krishnamurti, T. N., G. D. Rohaly, and H. S. Bedi, 1994: On the improvement of precipitation forecast skill from physical initialization. *Tellus,* **46A,** 598–614.
Kummerow, C., W. S. Olson, and L. Giglio, 1996: A simplified scheme for obtaining precipitation and vertical hydrometeor profiles from passive microwave sensors. *IEEE Trans. Geosci. Remote Sens.,* **34,** 1213–1232.
Lau, K. M., and P. H. Chan, 1986: The 40–50 day oscillation and the El Niño/Southern Oscillation: A new perspective. *Bull. Amer. Meteor. Soc.,* **67,** 533–534.
——, and L. Peng, 1987: Origin of low-frequency (intraseasonal) oscillations in the tropical atmosphere. Part I: The basic theory. *J. Atmos. Sci.,* **44,** 950–972.
——, and P. H. Chan, 1988: Intraseasonal and interannual variations of tropical convection: A possible link between the 40-day mode and ENSO. *J. Atmos. Sci.,* **45,** 950–972.
Lin, X., and R. H. Johnson, 1996: Heating, moistening, and rainfall over the western Pacific warm pool during TOGA COARE. *J. Atmos. Sci.,* **53,** 3367–3383.
Lojou J.-Y., R. Bernard, and L. Eymard, 1994: A simple method for testing brightness temperatures from satellite microwave radiometers. *J. Atmos. Oceanic Technol.,* **11,** 387–400.
McBride, J. L., N. E. Davidson, K. Puri, and G. C. Tyrell, 1995: The flow during TOGA COARE as diagnosed by the BMRC Tropical Analysis and Prediction System. *Mon. Wea. Rev.,* **123,** 717–736.
Miller, E., 1994: TOGA COARE Integrated Sounding System Data Rep. Vol. 1–9, 799 pp. [Available from Surface and Sounding Systems Facility, NCAR, P.O. Box 3000, Boulder, CO 80307.]
Mugnai, A., and E. A. Smith, 1988: Radiative transfer to space through a precipitating cloud at multiple microwave frequencies. Part I: Model description. *J. Appl. Meteor.,* **27,** 1055–1073.
——, H. J. Cooper, E. A. Smith, and G. J. Tripoli, 1990: Simulation of microwave brightness temperatures of an evolving hail storm at SSM/I frequencies. *Bull. Amer. Meteor. Soc.,* **71,** 2–13.
——, E. A. Smith, and G. J. Tripoli, 1993: Foundations for statistical–physical precipitation retrieval from passive microwave satellite measurements. Part II: Emission source and generalized weighting function properties of a time-dependent cloud-radiation model. *J. Appl. Meteor.,* **32,** 17–39.
Nakazawa, T., 1988: Tropical super-cluster under intraseasonal variation. Japan–U.S. Workshop on the ENSO Phenomena, University of Tokyo, Meteorology Rep. 88-1, Department of Meteorology, Geophysical Institute, 195 pp. [Available from Department of Meteorology, Geophysical Institute, University of Tokyo, Tokyo, Japan.]

Unauthenticated | Downloaded 12/05/23 04:44 PM UTC

Negri, A. J., and R. F. Adler, 1993. An intercomparison of three satellite infrared rainfall techniques over Japan and surrounding waters. *J. Appl. Meteor.,* **32,** 357–373.

Nitta, T., 1972: Energy budget of wave disturbances over Marshall Island during the year 1956 and 1958. *J. Meteor. Soc. Japan,* **50,** 71–84.

Panegrossi, G., and Coauthors, 1998: Use of cloud model microphysics for passive microwave-based precipitation retrieval: Significance of consistency between model and measurement manifolds. *J. Atmos. Sci.,* **55,** 1644–1673.

Parson, D., and Coauthors, 1994: The Integrated Sounding System: Description and preliminary observations from TOGA COARE. *Bull. Amer. Meteor. Soc.,* **75,** 553–567.

Puri, K., 1987: Some experiments on the use of tropical diabatic heating information for initial state specification. *Mon. Wea. Rev.,* **115,** 1394–1406.

Rasmusson, E. M., and P. A. Arkin, 1993: A global view of large-scale precipitation variability. *J. Climate,* **6,** 1495–1522.

Shinoda, T., and R. Lukas, 1995: Lagrangian mixed layer modeling of the western equatorial Pacific. *J. Geophys. Res.,* **100,** 2523–2541.

Short, D. A., P. A. Kucera, B. S. Ferrier, J. C. Gerlach, S. A. Rutledge, and O. W. Thiele, 1997: Shipboard radar rainfall patterns within the TOGA COARE IFA. *Bull. Amer. Meteor. Soc.,* **78,** 2817–2836.

Simpson, J., C. Kummerow, W.-K. Tao, and R. F. Adler, 1996: On the Tropical Rainfall Measuring Mission (TRMM) satellite. *Meteor. Atmos. Phys.,* **60,** 19–36.

Smith, E. A., and A. Mugnai, 1988: Radiative transfer to space through a precipitating cloud at multiple microwave frequencies. Part II: Results and analysis. *J. Appl. Meteor.,* **27,** 1074–1091.

——, and ——, 1989: Radiative transfer to space through a precipitating cloud at multiple microwave frequencies. Part III: Influence of large ice particles. *J. Meteor. Soc. Japan,* **67,** 739–755.

——, ——, H. J. Cooper, G. J. Tripoli, and X. Xiang, 1992a: Foundations for statistical-physical precipitation retrieval from passive microwave satellite measurements. Part I: Brightness temperature properties of a time dependent cloud-radiation model. *J. Appl. Meteor.,* **31,** 506–531.

——, X. Xiang, A. Mugnai, and G. Tripoli, 1992b: A cloud radiation model for spaceborne precipitation retrieval. *Extended Abstracts, Int. TRMM Workshop on the Processing and Utilization of the Rainfall Data Measured from Space,* Tokyo, Japan, Communications Research Laboratory, 273–283.

——, ——, ——, and ——, 1994a: Design of an inversion-based precipitation profile retrieval algorithm using an explicit cloud model for initial guess microphysics. *Meteor. Atmos. Phys.,* **54,** 53–78.

——, A. Mugnai, and G. Tripoli, 1994b: Theoretical foundations and verification of a multispectral, inversion-type microwave precipitation profile retrieval algorithm. *Proceedings of the ESA/NASA International Workshop on Microwave Radiometry,* B. J. Choudhury et al., Eds., VSP Science Press, 599–621.

——, C. Kummerow, and A. Mugnai, 1994c: The emergence of inversion-type precipitation profile algorithms for estimation of precipitation from satellite microwave measurements. *Remote Sens. Rev.,* **11,** 211–242.

——, X. Xiang, A. Mugnai, R. Hood, and R. W. Spencer, 1994d: Behavior of an inversion-based precipitation retrieval algorithm with high resolution AMPR measurements including a low frequency 10.7 GHz channel. *J. Atmos. Oceanic Technol.,* **11,** 858–873.

——, and Coauthors, 1998: Results of WetNet PIP-2 project. *J. Atmos. Sci.,* **55,** 1483–1536.

Smith, S. D., 1989: Water vapour flux at the sea surface. *Bound.-Layer Meteor.,* **47,** 277–293.

Stogryn, A., 1971: Equations for calculating the dielectric constant of saline water. *IEEE Trans. Microwave Theory Tech.,* **19,** 733–736.

——, 1972: The emissivity of sea foam at microwave frequencies. *J. Geophys. Res.,* **77,** 1658–1666.

Tao, W.-K., J. Simpson, S. Lang, M. McCumber, R. Adler, and R. Penc, 1990: An algorithm to estimate the heating budget from vertical hydrometeor profiles. *J. Appl. Meteor.,* **29,** 1232–1244.

——, ——, C.-H. Sui, B. Ferrier, S. Lang, J. Scala, M.-D. Chou, and K. Pickering, 1993a: Heating, moisture, and water budgets of tropical and midlatitude squall lines: Comparison and sensitivity to longwave radiation. *J. Atmos. Sci.,* **50,** 673–690.

——, S. Long, J. Simpson, and R. Adler, 1993b: Retrieval algorithms for estimating the vertical profiles of latent heat release: Their applications for TRMM. *J. Meteor. Soc. Japan,* **71,** 685–700.

Tripoli, G. J., 1992a: A nonhydrostatic model designed to simulate scale interaction. *Mon. Wea. Rev.,* **120,** 1342–1359.

——, 1992b: An explicit three-dimensional nonhydrostatic numerical simulation of a tropical cyclone. *Meteor. Atmos. Phys.,* **49,** 229–254.

Weare, B. C., 1989: Uncertainties in estimates of surface heat fluxes derived from marine reports over the tropical and subtropical oceans. *Tellus,* **41A,** 357–370.

Webster, P. J., 1983: Large-scale structure of tropical atmosphere. *Large-Scale Dynamical Processes in the Atmosphere,* B. J. Hoskins and R. P. Pearce, Eds., Academic Press, 235–275.

——, and R. Lukas, 1992: TOGA COARE: The Coupled Ocean–Atmosphere Response Experiment. *Bull. Amer. Meteor. Soc.,* **73,** 1377–1416.

Wilheit T. T., A. T. C. Chang, and L. S. Chiu, 1991: Retrieval of monthly rainfall indices from microwave radiometric measurements using probability distribution functions. *J. Atmos. Oceanic Technol.,* **8,** 118–1136.

——, and Coauthors, 1994: Algorithms for the retrieval of rainfall from passive microwave measurements. *Remote Sens. Rev.,* **11,** 163–194.

Xiang, X., E. A. Smith, and C. G. Justus, 1994: A rapid radiative transfer model for reflection of solar radiation. *J. Atmos. Sci.,* **51,** 1978–1988.

Yanai, M., S. Esbensen, and J. H. Chu, 1973: Determination of bulk properties of tropical cloud clusters from large-scale heat and moisture budgets. *J. Atmos. Sci.,* **30,** 611–627.

Yang, S., 1996: Four dimensional heat and moisture budgets derived from radiosonde and SSM/I measurements. Ph.D. dissertation, The Florida State University, 189 pp.

——, and E. Smith, 1999: Vertical structure and transient behavior of convective-stratiform heating in TOGA COARE from combined satellite-sounding analysis. *J. Appl. Meteor.,* in press.

Unauthenticated | Downloaded 12/05/23 04:44 PM UTC